

# 1 Intrinsic and extrinsic inhibition of cortical flow underlies 2 symmetry breaking during unilateral cytokinesis

3

4 **-Author names and Affiliations**

5 Christina Rou Hsu<sup>1,2</sup>, Gaganpreet Sangha<sup>1,2</sup>, Wayne Fan<sup>1,2</sup>, Joey Zheng<sup>1,2</sup>, and Kenji  
6 Sugioka<sup>1,2\*</sup>

7 <sup>1</sup>Life Sciences Institute, The University of British Columbia, 2350 Health Sciences Mall,  
8 Vancouver, BC V6T1Z3, Canada

9 <sup>2</sup>Department of Zoology, The University of British Columbia, 2350 Health Sciences  
10 Mall, Vancouver, BC V6T1Z3, Canada

11

12 **\*Corresponding author**

13 Kenji Sugioka

14 Life Sciences Institute, Department of Zoology, The University of British Columbia,  
15 2350 Health Sciences Mall, Vancouver, BC V6T1Z3, Canada

16 [sugioka@zoology.ubc.ca](mailto:sugioka@zoology.ubc.ca)

17 Phone: +1-604-404-3150

18

19

20

# 1 Short title

2 Symmetry breaking in unilateral cytokinesis

3

# 4 Summary

5 Eccentric closure of the contractile ring, known as unilateral cytokinesis, often orients  
6 along the body axis to maintain tissue integrity. Despite the identification of unilateral  
7 cytokinesis regulators, the mechanism of initial symmetry breaking remains elusive.  
8 Here, we report that intrinsic and extrinsic inhibition of cortical flow breaks cytokinesis  
9 symmetry in *Caenorhabditis elegans*. By coupling high-resolution 4D imaging with an *in*  
10 *vitro* cell contact reconstitution assay, we found that unilateral cytokinesis of the zygote  
11 P<sub>0</sub> and the two-cell stage blastomere AB are regulated by actin-dependent and adhesion-  
12 dependent mechanisms, respectively. Intracellular compression and intercellular adhesion  
13 in P<sub>0</sub> and AB, respectively, locally inhibited both furrow-directed cortical flow and  
14 cleavage furrow ingression, resulting in eccentric ring closure. Our study demonstrates  
15 that local mechanical suppression of ring-dependent cell cortex pulling is a common  
16 symmetry-breaking cue underlying multiple modes of unilateral cytokinesis.

17

18 **Keywords:** Cytokinesis, cortical flow, C. elegans, Contractile ring, Coronin, Anillin,  
19 Actin, Myosin, Cell division

20

# 1 Introduction

2 The contractile ring is a supramolecular structure critical for the physical partitioning of  
3 dividing cells, but its function is not limited to cell proliferation. In animal zygotes and  
4 epithelial tissues, contractile ring closure is often eccentric and is termed unilateral or  
5 asymmetric cytokinesis (Rappaport, 1996; Sugioka, 2021; Thieleke-Matos et al., 2017).  
6 Its disruption has been associated with cytokinesis failure and epithelial sheet and tube  
7 morphogenesis defects (Herszterg et al., 2013; Maddox et al., 2007; Taulet et al., 2017).  
8 Despite its developmental significance, the mechanism of unilateral cytokinesis remains  
9 unclear on several points.

10 A classically-known symmetry-breaking cue of unilateral cytokinesis is mitotic  
11 spindle positioning, which is critical for specifying contractile ring assembly at the  
12 equator of the cell cortex (Rappaport, 1986; Rappaport and Conrad, 1963). Central to  
13 contractile ring formation is the activation of the small GTPase RhoA (Figure. 2A)  
14 (Basant and Glotzer, 2018). Upon anaphase onset, the chromosome passenger complex  
15 recruits centralspindlin to the spindle midzone and activates oligomerization (Basant et  
16 al., 2015; Douglas et al., 2010). Centralspindlin then activates Ect2 RhoGEF, which in  
17 turn facilitates the formation of the active GTP-bound form of RhoA at the equatorial cell  
18 cortex (Gómez-Cavazos et al., 2020; Somers and Saint, 2003; Tatsumoto et al., 1999;  
19 Yüce et al., 2005). RhoA then stimulates downstream Rho-kinase and the actin  
20 nucleating/polymerizing factor formin to promote myosin II activation and F-actin  
21 assembly, respectively (Matsumura, 2005; Otomo et al., 2005). Pioneering studies have  
22 shown that the asymmetric positioning of the mitotic spindle, with the spindle midzone  
23 closer to one side of the equatorial cortex, is sufficient to induce unilateral cleavage in

1 ctenophore zygotes and normally symmetrically dividing sea urchin embryos (Rappaport  
2 and Conrad, 1963; Yatsu, 1912). The off-center spindle induces asymmetric activation of  
3 RhoA in the adjacent cell cortex (Bement et al., 2005). Thus, the geometric relationship  
4 between the equatorial cortex and mitotic spindle is a symmetry-breaking cue of  
5 unilateral cytokinesis in some animals, hereafter called spindle-dependent unilateral  
6 cytokinesis. However, spindle-cortex proximity does not explain unilateral cytokinesis in  
7 many tissues.

8       Epithelial cells undergo adherens junction-dependent unilateral cytokinesis. The  
9 mitotic spindle is slightly nearer to the apical cell cortex, but the furrow is usually formed  
10 from the basal side (Fleming et al., 2007; Morais-de-Sá and Sunkel, 2013; Nakajima et  
11 al., 2019; Woolner and Papalopulu, 2012). Inhibition of contractile ring components such  
12 as anillin and septin does not affect ring eccentricity, but knockdown of adherens junction  
13 components results in concentric contractile ring closure in *Drosophila* embryonic and  
14 follicular epithelia (Guillot and Lecuit, 2013; Morais-de-Sá and Sunkel, 2013). Although  
15 it has been reported that the mechanical resistance imposed by adherens junctions  
16 anchors the contractile ring at the apical cortex (Guillot and Lecuit, 2013), the  
17 relationship between junctions, cell-cortex dynamics, and furrow ingression remains  
18 unclear.

19       In contrast with the systems described above, *Caenorhabditis elegans* zygotes  
20 undergo adhesion-independent unilateral cytokinesis. Mitotic spindle positioning is not  
21 particularly off-center, while cortical components, including myosin, anillin, and septin,  
22 are enriched in the fast-closing furrow, forming a structurally asymmetric ring (Maddox  
23 et al., 2007). Unlike in *Drosophila* epithelial cells, anillin and septin are required for

structural asymmetry and unilateral cleavage. Recent studies have also revealed the significance of the concerted movement of cell-cortex material, or cortical flow, during this process (Figure 2A). Furrow-directed cortical flow compresses the cell cortex along the axis perpendicular to the contractile ring and facilitates F-actin alignment and myosin enrichment (Khaliullin et al., 2018; Reymann et al., 2016). Formin also reinforces F-actin alignment through a filament-guided filament assembly mechanism (Li and Munro, 2021). Importantly, ring constriction further pulls the cell cortex toward the equator, producing a positive-feedback loop between cortical flow and ring constriction (Khaliullin et al., 2018). Because asymmetric myosin enrichment, eccentric closure, and asymmetric cell cortex compression have been reported to occur simultaneously (Khaliullin et al., 2018; Maddox et al., 2007), the initial mechanism by which symmetry is broken remains unclear.

In this study, we performed a comparative analysis of adhesion-dependent and adhesion-independent unilateral cytokinesis using *C. elegans* as a model system, to gain insights into a unified mechanism underlying these seemingly very distinct division modes. Although implicated in the previous studies, there is no concrete evidence supporting adhesion-dependent unilateral cytokinesis in *C. elegans* (Bourdages et al., 2014; Koyama et al., 2012). Using blastomere isolation assays, high-resolution 4D imaging, and *in vitro* cell-contact reconstitution assays, we have identified symmetry-breaking cues.

# 1    **Results**

## 2    **High-resolution 4D imaging and quantitative analysis of contractile ring dynamics**

3    To understand the symmetry-breaking mechanism of unilateral cytokinesis, we  
4    performed the high-resolution 4D imaging of GFP-fused non-muscle myosin II (NMY-2)  
5    (Figure 1A, Figure S1A). Although imaging methods widely adopted in the *C. elegans*  
6    cytokinesis field slightly compress embryos to facilitate visualization of the cell cortex  
7    (Khaliullin et al., 2018; Li and Munro, 2021; Reymann et al., 2016), compression is  
8    known to induce global cortical rotation along the short axis of the cell (Schonegg et al.,  
9    2014; Singh et al., 2019) (Figure S1B). Compression-induced cortical rotation alters the  
10    positioning of fast- and slow-closing (leading and lagging, respectively) cortical sides  
11    between pre- and mid-cytokinesis, preventing the analysis of initial symmetry breaking.  
12    To avoid compression, we used cell-sized polystyrene beads as spacers between the  
13    coverslip and slide. Furthermore, we used a refractive index-matching medium and a  
14    silicone-immersion objective to reduce spherical aberration (Xiong and Sugioka, 2020)  
15    (Figure S1A).

16        These improvements enabled us to capture complete uncompressed embryonic  
17    volumes every 5.6 sec at a 1- $\mu$ m step size (a total of 31 Z slices), which are two- and  
18    five-fold increases of volumetric information and temporal resolution of the ring closure,  
19    respectively, compared to the previous state-of-the-art analysis of compressed embryos  
20    (Figure. 1A, Figure S2A, Movie S1) (Khaliullin et al., 2018). As expected, we did not  
21    observe cortical rotation (Figure S1B, Movie S1). We first analyzed zygote P<sub>0</sub> cells using  
22    an image analysis pipeline that measured the centroid and radius of the contractile ring at  
23    a given time from thousands of raw images (Figure. 1B, Figure S1A, S1C). From these

1 data, we calculated ring closure indices and ring eccentricities. Using an initial ring radii  
2  $R_0$  and at a given time  $R_t$ , the ring closure index  $f(t)$  was defined as:

$$3 \quad f(t) = (R_0 - R_t)/R_0 \quad (1)$$

4 We defined ring eccentricity  $g(t)$  using  $Q_t$ , the distance between the centroids of the  
5 initial ring ( $C_0$ ) and the ring at time  $t$  ( $C_t$ ), as:

$$6 \quad g(t) = Q_t/R_0 \quad (Q_t \leq R_0 - R_t) \quad (2)$$

7 The upper limit of the eccentricity at a given time point  $s(t)$  was limited by  $R_t$ , as:

$$8 \quad s(t) = \frac{R_0 - R_t}{R_0} = f(t) \quad (3)$$

9 Because  $s(t)$  is equal to  $f(t)$ , eccentricity cannot not exceed the ring closure index at any  
10 time (Figure. 1C and Movie S1). After analyzing multiple embryos, individual ring  
11 constriction curves versus time were aligned relative to the time at which the ring closure  
12 first exceeded 2% (Figure S1D); this allows us to detect differences in sub-percentage  
13 ring closure indices. We defined cytokinesis onset as the 17 sec before 2% ring closure,  
14 based on the extrapolation of a line passing two data points before the 2% ring closure to  
15 0 (Figure S1D). Our data alignment method was set to understand early symmetry-  
16 breaking events. While different from the method reported by Khaliulin et al. (2018)  
17 (Khaliullin et al., 2018), nevertheless, our data are in good agreement with theirs, as  
18 shown in Figure S2. On the other hand, our data include an additional 50–80 sec  
19 preceding 0% closure, which was not included by Khaliulin et al. (2018). Thus, our  
20 method allows analysis of early cortical dynamics of the uncompressed embryo at high  
21 temporal resolution while preserving the initial positioning of both leading and lagging  
22 cortices, which is necessary to understand the symmetry-breaking mechanism.

23

# **1 Intrinsic and extrinsic control of unilateral cytokinesis in P<sub>0</sub> and AB blastomeres**

2 We found that the P<sub>0</sub> contractile ring initially underwent nearly the upper limit of  
3 eccentric closure (Figure. 1C,  $f(t) = g(t)$ ; Movie S1). The observed maximum ring  
4 eccentricity represents dominant furrow ingression from the leading cortex. Unilateral  
5 furrow ingression continued until approximately 89 sec after the cytokinesis onset  
6 (Figure. 1B, C; left panel). After this time point, the lagging cortex gradually started  
7 ingression, reducing eccentricity (Figure 1C,  $f(t) > g(t)$ ; Movie S1).

8 Next, to understand a unified mechanism underlying adhesion-dependent and -  
9 independent unilateral cytokinesis, we sought an adhesion-mediated unilateral  
10 cytokinesis in *C. elegans* embryo. We focused on the two-cell stage AB blastomere that  
11 undergoes unilateral cytokinesis (Figure. 1A) (Ozugergin et al., 2022). In intact embryos,  
12 the AB contractile ring initially exhibited low eccentricity, resulting in more symmetric  
13 ring closure (Figure. 1B, C; middle panel). However, as the ring constricted, eccentricity  
14 gradually increased. The distinct contractile ring dynamics in P<sub>0</sub> and AB indicated a  
15 qualitative difference in the unilateral cytokinesis mechanisms. To test the requirement  
16 for adhesion in AB unilateral cytokinesis, we isolated the AB cell by mechanically  
17 separating it from the neighboring P<sub>1</sub> cell. Obtained isolated AB cells exhibited  
18 symmetric ring closure, suggesting that AB unilateral cytokinesis is adhesion-dependent,  
19 as in *Drosophila* epithelial cells (Guillot and Lecuit, 2013; Morais-de-Sá and Sunkel,  
20 2013).

21

22 **Lack of asymmetries in mitotic spindle positioning, RhoA activity, and myosin level**  
23 **at the beginning of P<sub>0</sub> and AB cytokinesis**



1 To address symmetry-breaking mechanisms in P<sub>0</sub> and AB cells, we first tested the  
 2 asymmetric regulation of known contractile ring assembly pathways (Figure. 2A). First,  
 3 we tested asymmetry in mitotic spindle positioning, a known symmetry-breaking cue in  
 4 in ctenophore zygotes (Rappaport and Conrad, 1963; Yatsu, 1912). A previous study  
 5 reported symmetric spindle positioning in P<sub>0</sub> (Maddox et al., 2007). To analyze both P<sub>0</sub>  
 6 and AB cells, we measured distances between centrosomes and leading (LE) and lagging  
 7 cortices (LG), calculating ratios of LE to LG (Figures 2B, 2C, and S3A). In both P<sub>0</sub> and  
 8 AB cells, the LE/LG ratio was close to 1.0, indicating mitotic spindle position symmetry  
 9 relative to leading and lagging cortices. These results confirm that the geometric  
 10 relationship between the mitotic spindle and cell cortex is not a symmetry-breaking cue  
 11 in these cell types.

12 Next, we examined the asymmetry of RhoA activity and myosin enrichment. To  
 13 monitor the former, we used a RhoA biosensor with a GFP fused to the C-terminus of  
 14 anillin containing conserved region (AH) and pleckstrin homology (PH) domains (Tse et  
 15 al., 2012). Ratios between leading and lagging cortices were quantified as shown in  
 16 Figure S3B. Both kymographs of the equatorial cortex and leading/lagging ratios (Figure  
 17 2D and E) show that both myosin enrichment and RhoA activity started to become  
 18 asymmetric after at least 50 sec from the onset of cytokinesis. Since both were symmetric  
 19 at the beginning of P<sub>0</sub> and AB cytokinesis, asymmetric myosin enrichment and RhoA  
 20 activity do not appear to cause early symmetry breaking.

21

22 **Actin alignment asymmetry specifies ring closure direction in P<sub>0</sub> cells**

1 To test for actin alignment asymmetry in P<sub>0</sub> cells, we imaged whole Lifeact::mKate2-  
 2 expressing embryos as described above (Figure 3A). For the analysis of actin filament  
 3 orientation, we selected embryos that underwent furrow ingression perpendicular to the  
 4 imaging plane, to have either a leading or lagging cortex at the surface of the image stack.  
 5 For each embryo, ten surface slices closer to the objective lens were flattened by  
 6 summation; only a central 9 × 9-μm region was analyzed to avoid deformation of the  
 7 filament structure at the high-curvature surface (white dotted box in Figure 3A). Actin  
 8 filament orientations were estimated based on the gradient structure tensor in a local area,  
 9 as previously described (Figure 3B, yellow lines) (Püspöki et al., 2016). We found that  
 10 the circular means of actin filament orientation at the lagging cortex were significantly  
 11 higher than those at the leading cortex (Figure 3C). Strikingly, asymmetry was first  
 12 observed approximately 55 sec before cytokinesis onset. In contrast, the actin signal  
 13 intensity was not asymmetric (Figure 3D). These results suggest that actin alignment  
 14 asymmetry specifies leading and lagging cell cortices in P<sub>0</sub> cells.

15 To examine a requirement for actin regulations in unilateral cytokinesis, we  
 16 inhibited actin and actin binding proteins. A pioneering study has shown that ANI-  
 17 1/anillin is essential for unilateral cytokinesis (Maddox et al., 2007). We confirmed that  
 18 *ani-1(RNAi)* caused concentric ring closure (Figure 3E-G). However, as anillin is a  
 19 scaffold protein that interacts with F-actin, myosin II, RhoA, phosphatidylinositol, and  
 20 microtubules (Liu et al., 2012; van Oostende Triplet et al., 2014; Piekny and Glotzer,  
 21 2008), the significance of anillin-dependent F-actin regulation in unilateral cytokinesis is  
 22 unclear. Partial knockdown of the actin nucleator and polymerizing factor CYK-1/formin  
 23 has been also reported to result in symmetric cytokinesis at the end of contractile ring

1 closure, based on 2D analyses of compressed embryos (Chan et al., 2019), but we did not  
2 observe early unilateral cytokinesis defects in our 4D analysis of uncompressed embryos  
3 (Figure 3G).

4 To further investigate a requirement for actin organization in unilateral  
5 cytokinesis, we inhibited or knocked down additional actin regulators. The Arp2/3  
6 complex mediates actin nucleation from existing filaments, leading to branched network  
7 assembly (Goley and Welch, 2006). POD-1/coronin is a negative regulator of Arp2/3 that  
8 promotes actin debranching by removing Arp2/3 from F-actin (Xie et al., 2021). Finally,  
9 we used a semi-dominant negative, temperature-sensitive mutant of one of *C. elegans*  
10 actin encoding genes, *act-2*. The *act-2(or295ts)* is a missense G14R mutation near the  
11 conserved ATP-binding pocket, and causes abnormal actin distribution (Willis et al.,  
12 2006). We found that both *pod-1(RNAi)* and *act-2(or295ts)* resulted in more symmetric  
13 contractile ring closure (Figure 3E-G). In contrast, knockdown of the Arp2/3 complex did  
14 not affect cytokinesis asymmetry, consistent with a previous report in compressed  
15 embryos (Chan et al., 2019). Ring eccentricity has been shown to be insensitive to the  
16 reduction of myosin activity (Maddox et al., 2007). Consistently, the knockdown of LET-  
17 502/Rho kinase did not cause unilateral cytokinesis defects (Figure 3E-G). However, a  
18 strong reduction in myosin activity by the knockdown of myosin light chain MLC-4  
19 resulted in symmetric closure (Figure 3E, G). Thus, regulation of both actin and myosin  
20 is required for unilateral cytokinesis.

21

22 **Compression of the lagging cortex along the axis of the contractile ring in P<sub>0</sub> cells**

1 We hypothesized that the cell cortex with asymmetric actin alignment underwent  
 2 anisotropic contraction. To test this hypothesis, we measured cortical flow using particle  
 3 image velocimetry (PIV) (Thielicke and Sonntag, 2021) (Figure 4A). We analyzed the  
 4 maximum projection of the top 15 slices seen from the leading, lateral, and lagging  
 5 cortices (Movie S2). To quantify cortical dynamics, we calculated the convergence of  
 6 PIV vectors per area along the axis of the contractile ring and the axis perpendicular to it  
 7 (Figure 4B). This represents an advantage of uncompressed imaging since previous  
 8 studies did not report ring axis convergence, presumably due to the compression-  
 9 dependent cortical rotation. Positive and negative convergence indicated the influx and  
 10 efflux of cortical material, respectively. It is important to note that convergence can be  
 11 interpreted as compression before furrow ingression (Figure 4C, left). After furrow  
 12 ingression onset, convergence indicates both compression and ingression (cortical  
 13 material moving away vertically from the imaging plane) (Figure 4C, right). We used the  
 14 lateral cortex view to produce average flow vector and convergence maps (Figure 4D and  
 15 Movie S3) and the leading and lagging cortex views to quantify convergence at the cell  
 16 equator (Figure 4E).

17 First, we compared perpendicular axis convergence between leading and lagging  
 18 cortices (Figure 4D, bottom row; Figure 4E, left graph; Movie S3). Before and until 11  
 19 sec following cytokinesis onset, perpendicular-axis convergence was positive at both the  
 20 leading and lagging cortices, indicating that they are being compressed symmetrically  
 21 (Figure 4D and E, -75–11 sec). At 16 sec after cytokinesis onset, perpendicular axis  
 22 convergence started to increase at the leading cortex while decreasing at the lagging  
 23 cortex (Figure 4D and 4E, 16–84 sec). These results are in agreement with those from

1 slightly compressed embryos (Khaliullin et al., 2018). The same study showed that the  
2 contractile ring pulls on the cortical surface from a relatively polar area at a rate  
3 proportional to the amount of ring myosin. Consistently, the elevation of the  
4 perpendicular-axis convergence at the lagging cortex coincides with its ingression-onset  
5 (Figure 4E; left graph, ~ 84 sec as estimated by the separation of  $f(t)$  and  $g(t)$  curves in  
6 Figure 1C). Because initial asymmetry in perpendicular axis convergence emerged after  
7 cytokinesis onset, it is less likely to be an ingression symmetry-breaking cue.

8       Next, we compared ring axis convergence between the leading and lagging  
9 cortices. We found that it was higher at the lagging cortex before cytokinesis onset, with  
10 positive convergence persisting until after furrow ingression onset of the lagging cortex  
11 (Figure 4E; right graph, -75–125sec, and Figure 4F). These results suggest that the  
12 lagging equatorial cortex is compressed along the contractile-ring axis in  $P_0$  cells. The  
13 compression at the lagging cortex was in agreement with the biased F-actin orientation  
14 along the ring axis.

15

## 16 **Ring axis compression limits cleavage furrow ingression in $P_0$ cells**

17 Positive cortical convergence was observed in the lagging cortex before and during  
18 cytokinesis. Thus, we hypothesized that cortical compression inhibits ring ingression  
19 during cytokinesis. To test this, we employed the *act-2(or295ts)* mutant, which  
20 occasionally exhibits the ring oscillation phenotype (67%,  $n = 15$ ) while retaining the  
21 normal contractile ring closure rate (Figure 5A). We found that *act-2(or295ts)* exhibited  
22 higher cortical contractility than the control, as determined by the pronounced repetition  
23 of coalescence and dissipation of myosin clusters (Figure 5B). We then compared the

1 relationship between cortical compression and the furrow ingression using the maximum  
 2 projection image of the focal planes closer to the objective lens (Figure 5C and 5D, top  
 3 surface) and the ring en face view (Figure 5C and 5E) from the same embryo. We found  
 4 that contraction at the top surface coincided with the immobilization of the top furrow  
 5 (Figure 5D-F; 73–84 sec and 106–117sec; Movie S4). In contrast, cortical relaxation  
 6 coincided with furrow ingression from the top (Figure 5D-F, 95 sec; Movie S4). We  
 7 measured the correlation between ring velocity and ring convergence (Figure 5G, time  
 8 series of one sample). Pearson’s coefficients of five embryos (Figure 5H) showed that  
 9 perpendicular axis convergence did not correlate with ring ingression. In contrast, ring  
 10 axis convergence was negatively correlated with ring ingression from the top surface  
 11 (Figure 5G). These results suggest that ring-axis compression inhibits furrow ingression  
 12 without affecting the rate of overall ring constriction.

13       Theoretical and experimental studies have shown that the contractile ring, with its  
 14 higher cortical tension, pulls in the cell cortex from the more relaxed polar region (Bray  
 15 and White, 1988; Greenspan, 1978; Khaliullin et al., 2018; Wolpert, 1960; Zinemanas  
 16 and Nir, 1987, 1988). Thus, we hypothesized that the ingression rate is determined by a  
 17 tug-of-war between cortical compression and contractile ring-dependent cell cortex  
 18 pulling. To test this, we measured myosin cluster displacement with respect to the timing  
 19 of peak compression (Figure 5I). We found that cortical myosin underwent isotropic  
 20 contraction while migrating toward the furrow during relaxation (Figure 5I, left two  
 21 panels). After cytokinesis, myosin clusters did not show biased movement toward the  
 22 furrow (Figure 5I, right panel). These results suggest that cortical compression inhibits  
 23 furrow ingression by suppressing furrow-directed cortical flow.

1

## 2 **Adhesion leads to resistance of cleavage furrow ingression in AB cells**

3 Next, we investigated the mechanisms underlying unilateral AB cytokinesis. First, we  
4 tested whether different molecular mechanisms are required in AB cells than in P<sub>0</sub> cells.  
5 We tested *act-2(or295ts)*, *ani-1(RNAi)*, and *pod-1(RNAi)*, all of which resulted in  
6 symmetric P<sub>0</sub> cytokinesis (Figure 3B). Interestingly, the contractile rings underwent  
7 eccentric closure in all three cases conditions, with proximity to the cell-cell boundary as  
8 in wild-type controls (Figure 6A). Although *pod-1(RNAi)* embryos exhibited the lowest  
9 ring eccentricity in P<sub>0</sub> cells (Figure 3G), they exhibited wild-type level eccentricity in AB  
10 cells (Figure 6B, C). These results suggest that AB unilateral cytokinesis is not sensitive  
11 to alternations in actin dynamics and is regulated by a different mechanism.

12 The AB cell underwent symmetric cytokinesis after removing the neighboring P<sub>1</sub>  
13 cell (Figure 1). There are two possible mechanisms underlying this type of unilateral  
14 cytokinesis. First, junctional proteins may suppress furrow ingression from the lagging  
15 cortex by controlling downstream intracellular signaling (e.g., RhoA inhibition). Second,  
16 adhesion may prevent furrow ingression mechanically. We tested the latter possibility  
17 using adhesive polystyrene beads that did not contain proteins.

18 We attached one or two adhesive beads to the isolated AB cell before anaphase  
19 onset to test the effects of different adhesion strengths on the contractile ring dynamics.  
20 After attaching an adhesive bead, the AB contractile ring initially underwent symmetric  
21 closure but gradually increased eccentricity in the middle of cytokinesis (Figure 6C-D).  
22 The contractile ring eventually returned to the cell center by the end of ring closure  
23 (Figure 6C, right graph; 6D). When attaching two adhesive beads, the contractile ring

1 also initially underwent symmetric closure, but ring eccentricity steadily increased until  
 2 the end of cytokinesis (Figure 6C and 6E). The dynamics in the AB cells attached by two  
 3 beads were similar to that of intact AB cells, wherein the ring initially closed  
 4 symmetrically but later steadily increased eccentricity until it plateaued (Figure 6B).  
 5 These results suggest that adhesion is sufficient to induce unilateral cytokinesis. We also  
 6 found that ring eccentricity was higher when a bead was attached to the equatorial cortex  
 7 rather than in the polar region (Figure 6F). Because the polar cortex undergoes relaxation  
 8 and actively loses actomyosin (Chapa-Y-Lazo et al., 2020), these data suggest the  
 9 importance of physical connectivity between adhesion, the plasma membrane, and the  
 10 cell cortex for the regulation of furrow ingression.

11 Finally, we measured angles of ingression at sites with and without an adhesive  
 12 bead, to assess the mechanical resistance of the cell cortex (Figure 6G). Ingression angles  
 13 were initially symmetric (Figure 6G, i). As the ring constricted, the angle of ingression  
 14 became overtly asymmetric, with higher and slower reduction rates at the adhesion-free  
 15 and adhering sites, respectively (Figure 6G, ii). When the ring further constricts, the cell  
 16 surface near it was locally detached from the adhesion site, leading to a rapid decrease in  
 17 the angle of ingression (Figure 6G, iii). These dynamics suggest three stages of the  
 18 adhesion-cortex relationship. First, adhesion imposes weak resistance against ring-  
 19 dependent cortex bending during the initial concentric closure observed in intact embryos  
 20 and in all *in vitro* experiments (Figure 6G, schematic i). Second, adhesion imposes  
 21 stronger resistance as the ring constricts, leading to eccentric closure in all the tested  
 22 cases (Figure 6G, schematic ii). Third, ring-dependent cell cortex pulling and a sudden  
 23 adhesion rupture resulted in the quick bending of the cortex and the ring returning to the



1 cell center when one adhesive bead was used (Figure 6G, schematic iii). Strong adhesion  
2 in intact and isolated AB cells attached by two beads prevented the premature release of  
3 ring anchoring, allowing eccentric ring positioning at the end of cytokinesis.

4

## 5 **Adhesion limits furrow-directed cortical flow**

6 We hypothesized that adhesion would inhibit ring-dependent cell cortex pulling. If this  
7 hypothesis is correct, the furrow-directed cortical flow should be limited by adhesion.  
8 Indeed, in our previous study on AB cell division axis orientation, we observed bead  
9 attachment-dependent suppression of furrow-directed cortical flow (Sugioka and  
10 Bowerman, 2018). However, in previous experiments, we did not rule out the possibility  
11 that physical contact, rather than adhesion, limits furrow-directed cortical flow.

12 Therefore, we measured furrow-directed cortical flow in the regions distal and proximal  
13 to the bead contact site using beads of different sizes (Figure 7A). We found that furrow-  
14 directed cortical flow was reduced at the cortex proximal to the contact site in a bead  
15 diameter-dependent manner (Figure 7B, C). Taken together, these results indicate that  
16 adhesion limits furrow-directed cortical flow by suppressing ring-dependent cell cortex  
17 pulling.

18

## 19 **Discussion**

20 Although spindle off-centering is a known symmetry-breaking cue for unilateral  
21 cytokinesis in ctenophore zygotes and manipulated sea urchin embryos (Bement et al.,  
22 2005; Rappaport and Conrad, 1963; Yatsu, 1912), the mechanism underlying spindle-  
23 independent symmetry breaking was unclear before this study. The two important model

1 systems, i.e., *C. elegans* P<sub>0</sub> and *Drosophila* epithelial cells, have very distinct molecular  
 2 requirements: the former is adhesion-independent but anillin-septin-dependent, while the  
 3 latter is adhesion-dependent but anillin-septin-independent (reviewed in Sugioka, 2021).  
 4 In this study, we identified adhesion-dependent unilateral cytokinesis in *C. elegans* AB  
 5 cells and performed a comparative analysis of adhesion-dependent and adhesion-  
 6 independent unilateral cytokinesis.

7       Based on our analyses, we propose a unified symmetry-breaking mechanism  
 8 underlying adhesion-independent and adhesion-dependent unilateral cytokinesis (Figure  
 9 7D). Since both ring-axis compression and adhesion suppressed the furrow ingression as  
 10 well as furrow-directed cortical flow, it is likely that they inhibited ring-dependent cortex  
 11 pulling (Figure 7D, middle box). During migration from the cell surface into the division  
 12 plane, the cell cortex changes its curvature (Figure 7D, top-right diagrams). Ring-axis  
 13 compression should increase cortical stiffness by requiring more energy for the ring to  
 14 deform the cell cortex to pull in. In contrast, adhesion externally inhibits ring-dependent  
 15 cortex pulling by imposing mechanical resistance. Adhesion also induces myosin  
 16 inhibition in this cell type and may prevent furrow-directed cortical flow (Sugioka and  
 17 Bowerman, 2018). This mechanical suppression model is consistent with that proposed  
 18 for *Drosophila* embryonic epithelial cells (Guillot and Lecuit, 2013), but our study  
 19 further characterized the spatiotemporal ring-cortex interaction and expanded its utility to  
 20 the nonadhesive and nonepithelial cells. In summary, our findings indicate that intrinsic  
 21 and extrinsic regulation of local cortical stiffness is a common symmetry-breaking cue  
 22 for spindle geometry-independent unilateral cytokinesis.

1           This intrinsic and extrinsic control of local cortical stiffness can explain the  
2   distinct contractile ring trajectories observed *in vivo* and *in vitro* (Figure 7D, bottom-right  
3   panels). In P<sub>0</sub> cells, the cell cortex was already stiffer than the other areas before  
4   cytokinesis onset (preconditioning), leading to maximum eccentricity from the early  
5   phase of cleavage (Figure 7D, schematic i). The subsequent suppression of ring-axis  
6   compression allowed lagging cortex ingression and a reduction in eccentricity (Figure  
7   4E). The oscillatory ring trajectory in *act-2(or295ts)* is likely due to oscillatory cortical  
8   compression, as shown in Figure 5 (Figure 7D, schematic ii). In the AB cell, adhesion did  
9   not impose strong mechanical resistance at the beginning, presumably owing to the  
10   typical strain-stress relationship, then gradually increases resistance to cause eccentric  
11   closure (Figure 7D, schematic iii). When adhesion was weak, adhesion rupture reduced  
12   ring eccentricity (Figure 7D, schematic iv). Taken together, a few simple rules can  
13   generate diverse ring trajectories; therefore, this knowledge will be useful for estimating  
14   spatial cytokinesis control in more complex tissues.

15           One notable difference among tissues undergoing spindle-independent unilateral  
16   cytokinesis is the spatial organization of the contractile ring. Asymmetric myosin  
17   enrichment at the leading edge has been observed in *C. elegans* P<sub>0</sub> and AB cells and  
18   *Drosophila* pupal dorsal thorax epithelial cells (this study; Founounou et al., 2013;  
19   Herszterg et al., 2013; Maddox et al., 2007) but not in *Drosophila* embryonic epithelia,  
20   follicular epithelia, and pupal wing epithelia (Guillot and Lecuit, 2013; Herszterg et al.,  
21   2013; Morais-de-Sá and Sunkel, 2013). Importantly, cortical stiffness-dependent  
22   suppression of ring-dependent cortex pulling can account for the asymmetric ingression  
23   of both structurally asymmetric and symmetric contractile rings (this study; Guillot and

1 Lecuit, 2013). This observation is consistent with our model, in which mechanical  
2 suppression occurs upstream of compression-dependent feedback (Figure 7D). We  
3 speculate that the above-described tissues are only different in terms of their downstream  
4 myosin enrichment mechanisms: structurally asymmetric and symmetric rings rely more  
5 on compression feedback and RhoA pathways, respectively.

6 By integrating our results and the above discussion, we predict that the ring-  
7 dependent cortex pulling is tuned differently in different tissues to execute tissue-specific  
8 morphogenic cytokinesis. Three important parameters are the strength of compression-  
9 dependent myosin recruitment to the ring, RhoA-dependent myosin recruitment to the  
10 ring, and cortical stiffness. Compression-dependent myosin enrichment should translate  
11 subtle cortical stiffness asymmetry into increased ingression rate difference by forming a  
12 structurally asymmetric contractile ring. For a compression-dependent feedback  
13 mechanism to effectively create a structurally asymmetric contractile ring, RhoA-  
14 dependent myosin recruitment should be limited. Conversely, excessive RhoA-dependent  
15 myosin enrichment suppresses ring-dependent mechanosensing of subtle cortical stiffness  
16 asymmetry. Understanding the tissue-specific ring-cortex relationship and its local tuning  
17 by RhoA activity or tissue mechanics is necessary to further delineate the role of  
18 cytokinesis in animal morphogenesis.

19

## 20 **Acknowledgements**

21 We thank the *Caenorhabditis* Genetics Center (funded by the NIH Office of Research  
22 Infrastructure Programs; P40 OD010440) for sharing *C. elegans* strains. We also thank  
23 Bruce Bowerman for providing valuable advice and Chris Doe for sharing lab equipment.

1 This work was supported by the Canadian Institutes of Health Research (Project Grant;  
2 PJT-169145), Government of Canada's New Frontiers in Research Fund (NFRFE-2019-  
3 00310), and the Health Research BC (Scholar Award; SCH-2020-0406) to K.S. C.R.H  
4 was supported by British Columbia Graduate Fellowship.

## 6 **Author contributions**

7 **C.R.H.:** Formal analysis, Investigation, Writing-Original Draft, Validation,  
8 Visualization. **G.S.:** Formal analysis, Investigation. **W.F.:** Formal analysis, Investigation.  
9 **J.Z.:** Formal analysis, Investigation. **K.S.:** Conceptualization, Formal analysis,  
10 Investigation, Methodology, Software, Validation, Writing-Original Draft, Writing-  
11 Review & Editing, Supervision, Funding acquisition.

## 13 **Declaration of interests**

14 The authors declare no competing interests.

# 1 **Materials and methods**

## 2 ***C. elegans* culture and strains**

3 All *C. elegans* strains were cultured using the standard method (Brenner, 1974). A  
4 temperature sensitive-actin mutant *act-2(or295)* was cultured at 15°C until the L4 larval  
5 stage and incubated at 25°C overnight before imaging. Lifeact::mKate2 strain was  
6 cultured at room temperature.

## 8 **RNAi**

9 Feeding RNAi was performed at 25°C using the standard method (Ahringer, 2006). For  
10 control RNAi, a bacterial strain carrying an empty vector (L4440) was used. For *cyk-1*,  
11 *arx-2*, *ani-1* and *let-502*, the L2 stage larvae were cultured on freshly prepared feeding  
12 RNAi plates on day 1. The L4 larvae were then transferred to new feeding RNAi plates  
13 on day 2 and imaged on day 3. For *pod-1* and *mlc-4*, L4 larvae were cultured on feeding  
14 RNAi plates and used for imaging on the next day.

## 16 **Blastomere isolation**

17 Blastomeres were isolated as described before (Hsu et al., 2019). We cut the gravid adult  
18 worms in egg salt buffer and treated them with hypochlorite solution [75% Clorox  
19 (Clorox) and 2.5N KOH] for 50 seconds. After washing twice with Shelton's growth  
20 medium (Shelton and Bowerman, 1996), embryos were transferred to fresh Shelton's  
21 growth medium. Eggshell and permeability barrier were removed by mouth pipetting  
22 with hand-drawn microcapillary tubes (10 microliters, Kimble Glass Inc.). The two-cell  
23 stage eggshell-free embryos were further pipetted to remove the cell-cell contact.

1

## 2 **Adhesive polystyrene bead preparation**

3 The detailed method is described in our previous papers (Hsu et al., 2019; Sugioka and  
4 Bowerman, 2018). 10 mg carboxyl-modified polystyrene beads with diameters of 30  $\mu\text{m}$   
5 (Kisker Biotech GmbH & Co.), 20  $\mu\text{m}$ , 10  $\mu\text{m}$ , and 4  $\mu\text{m}$  (Polysciences) were washed  
6 twice with 100 mM 2-(N-morpholino) ethanesulfonic acid (MES) buffer (pH6.5) and  
7 incubated with 1 mL MES buffer containing 10 mg 1-Ethyl-3-(3-dimethylaminopropyl)  
8 carbodiimide (EDAC) for 15 mins at room temperature. We washed the beads twice with  
9 phosphate buffered saline (PBS) and incubated them with 0.5 mL PBS containing 0.05  
10  $\mu\text{g}$  Rhodamine Red-X succinimidyl ester (ThermoFisher Scientific) for 5 minutes. The  
11 appropriate concentration was also determined by treating the beads with a series of  
12 serially diluted Rhodamine Red-X solution (Hsu et al., 2019). The beads were washed  
13 twice with PBS and stored in PBS at 4°C. Adhesiveness of the beads was confirmed by  
14 attaching them to the isolated blastomere using the mouse pipette. If successful, the  
15 adhesion is firmly established and cells do not dissociate spontaneously.

16

## 17 **Live-imaging sample preparation**

18 To obtain embryos, gravid adults were dissected on a coverslip, in a droplet of 10-12  $\mu\text{l}$   
19 of refractive index-matching medium (30% iodixanol diluted in egg salt buffer,  
20 supplemented with 30  $\mu\text{m}$  diameter plain polystyrene beads) as described before (Xiong  
21 and Sugioka, 2020). After placing the coverslip gently onto a slide glass, three edges of  
22 coverslip were sealed with petroleum jelly (Vaseline), with one edge remaining open to  
23 the air. We realized that this method improved the success rate of imaging for

1 inexperienced users. Inexperienced users may observe cell death due to the acute  
2 compression during the sample preparation and requires training using control strains. If  
3 all the processes were performed gently, the imaging condition does not have adverse  
4 effects on the embryonic viability, as judged by the normal cell division in the next cell  
5 cycle.

6

## 7 **Microscopy**

8 Intact embryos were imaged using a microscope Olympus IX83 (Olympus), equipped  
9 with a spinning-disk confocal unit CSU-W1 (Yokogawa), a scientific CMOS camera  
10 Prime 95B (Photometrics), a piezoelectric stage NANO-Z (Mad City Labs), a silicon  
11 immersion objective UPLSAPO60XS2 (NA1.3, 60X; Olympus), and a beam splitter  
12 Optosplit II (Cairn Research), which is controlled by Cellsense Dimension (Olympus). A  
13 silicone immersion oil (Z81114; refractive index: 1.406 at 23°C; Olympus) was used as  
14 an immersion medium. Samples were illuminated by diode-pumped lasers with 488 nm  
15 and 561 nm wavelengths, and the simultaneous two color-imaging was performed with  
16 150 msec camera exposure time, 1- $\mu$ m Z-step size with a total of 31 slices per frame, 5.6  
17 sec interval, and the duration of 15 mins. Isolated blastomeres were imaged using a  
18 microscope Leica DMI8 (Leica Microsystems), equipped with a spinning-disk confocal  
19 unit CSU-W1 with Borealis (Andor Technology), dual EMCCD cameras iXon Ultra 897  
20 (Andor Technology), and an oil-immersion PL APO objective lens (NA1.4, 63X; Leica),  
21 and controlled by Metamorph (Molecular Devices). Data in Figure 6D-G were imaged  
22 with 1.5  $\mu$ m Z-step size and 15 sec intervals. Data in Figure 7 were imaged with 1.5  $\mu$ m



1 Z-step size and 10 sec intervals, with only the half volume closure to the objective lens  
2 were imaged.

3

#### 4 **Quantification of the P<sub>0</sub> contractile ring dynamics**

5 Obtained 4D data were deconvoluted using a constrained iterative and advanced  
6 maximum likelihood algorithm (iteration: 5), using Olympus Cellsens software  
7 (Olympus, Inc). Each 4D tiff stack file was processed using Fiji (Schindelin et al., 2012)  
8 (Figure S1). The deconvoluted images were processed using Gaussian blur (sigma = 2)  
9 and an image J plug-in “attenuation correction” (opening =3, reference =15) (Biot et al.,  
10 2008). A 10 μm W x 32 μm H boxed region corresponding to the contractile ring was  
11 selected and adjusted for the fluorescence intensity so that the signal will not be saturated  
12 in the next step, and rotated by 3D projection (Brightest point, interpolation on). After  
13 selecting a plane of en face ring view, the images were segmented and quantified using  
14 an Image J plug-in Morpholib J (Legland et al., 2016). The segmented contractile ring  
15 areas were measured for ring radius, ring centroid, and ring angle. The radius of the  
16 segmented area was estimated using ellipsoid fitting and derived by calculating the  
17 average of major and minor radii of the ellipsoid. Data were aligned relative to the time  
18 point first exceeded 2% ring closure. The ring trajectory images were obtained with an  
19 in-house image J macro using same data.

20

#### 21 **Quantification of the AB contractile ring dynamics**

22 Since the AB cell undergoes rotation during its division, the precise quantification is  
23 challenging. We first selected samples undergoing unilateral cleavage roughly in parallel

1 to the imaging plane, and corrected for cell rotation using Stackreg plug-in of Image J  
2 using chromosome signal (polar bodies were deleted using a brush tool to avoid abnormal  
3 image registration) (Thévenaz et al., 1998). The rotation-corrected images were then  
4 processed by the same pipeline used for the P<sub>0</sub> cell.

5

## 6 **3D visualization and quantification of contractile ring dynamics in isolated** 7 **blastomeres**

8 The oblique view of cells in Figure 1A, Figure 6A, and Figure 6D were generated using  
9 an Image J plug-in Clear Volume (Royer et al., 2015). The analysis of the contractile ring  
10 dynamics in isolated blastomeres is challenging since the cell is rotated along different  
11 axes, and not all the planes were captured during imaging. Thus, we made en face ring  
12 view images for each time point using Clear Volume, and estimated the cell and ring  
13 contours, centroids, and diameters, by selecting more than four points along the cell and  
14 ring perimeter, respectively, using an Image J macro “Smallest Enclosing Circle”  
15 (Schindelin et al., 2012). The ring closure rate and eccentricity were calculated using the  
16 method described above for other cells. Measurements were performed three times per  
17 sample, and average values were used to mitigate the relatively higher error rate  
18 compared to the automatic segmentation method used for intact embryos.

19

## 20 **Kymographs**

21 Kymographs in Figure 2D were generated by stacking 1.5 μm W x 32 μm H rectangular  
22 regions at a given time along a user defined line passing the equatorial cortex or furrow  
23 using an in-house image J macro. Kymographs in Figure 5B were generated by stacking

1 49  $\mu\text{m}$  W x 1.8  $\mu\text{m}$  H boxes using Fiji (built-in function, Make Montage). Kymographs in  
2 Figure 5I were generated by stacking 11  $\mu\text{m}$  W x 3.7  $\mu\text{m}$  H rectangular regions  
3 corresponding to a myosin cluster. The timing is adjusted so that the peak myosin cluster  
4 intensity comes the 4th out of total 8 frames, using an in-house image J macro.

## 6 **Quantification of centrosome positioning**

7 For the  $P_0$  cell, obtained 4D images were rotated so that the angle of unilateral closure, at  
8 5% ring closure, is accurately in parallel to the imaging plane (Figure S3A). The  
9 distances between a centrosome and leading and lagging cortices were measured using an  
10 in-house image J macro. For the AB cell, we only used samples undergoing unilateral  
11 cleavage roughly in parallel to the imaging plane (Figure S3A). The distance between a  
12 centrosome and a line passing the both ends of the AB- $P_1$  cell boundary was measured to  
13 calculate the centrosome-lagging cortex distance. We then drew a line passing a  
14 centrosome, and being perpendicular to the above-described AB- $P_1$  boundary line. The  
15 intersection of this line and a line in parallel to the leading cortex was used to calculate  
16 the centrosome-leading cortex distance. Data were aligned relative to cytokinesis onset  
17 defined by the 4D ring dynamics data described above.

## 19 **Quantification of signal intensities**

20 To accurately measure the signal intensities within a thin layer of leading and lagging  
21 cortices, we selected embryos undergoing unilateral furrow ingression roughly in parallel  
22 to the imaging plane (Figure S3B). We selected a Z slice containing the center of  
23 contractile ring at about 200 second after cytokinesis onset, and calculated the summation

1 of three Z slices around the ring center. We then measured signal intensities in  $1.83 \mu\text{m} \times$   
 2  $0.55 \mu\text{m}$  boxes, corresponding to the cell cortex and the tip of the cleavage furrow before  
 3 and after cleavage onset, respectively.

4

## 5 **Quantification of the F-actin alignment**

6 The obtained 4D data sets of lifeact::mKate2-expressing embryos were deconvoluted and  
 7 analyzed to quantify ring closure dynamics by the above-described method using  
 8 Morpholib J. We selected embryos showing leading or lagging cell cortex closer to the  
 9 objective lens. For each data, ten slices at the cell surface closer to the objective lens were  
 10 flattened by summation using Fiji, and central  $9 \mu\text{m} \times 9 \mu\text{m}$  rectangular regions were  
 11 analyzed to avoid deformation of filament structure at the high-curvature surface. The  
 12 orientations of actin filaments were estimated based on the gradient structure tensor in a  
 13 local area using an Image J plug-in Orientation J (Gradient: Cubic Spline, local window:  
 14 2 pixel) (Püspöki et al., 2016). Circular mean was calculated using Scipy (Virtanen et al.,  
 15 2020) and the timings of data were aligned relative to cytokinesis onset.

16

## 17 **Visualization of F-actin alignment**

18 To visualize F-actin alignment in Figure 3A-B, the above-described flattened images  
 19 were processed using an unsharp mask (Image J built-in function) and an Image J plug-in  
 20 Feature J (Edges:, smoothing scale 1.0) (Meijering). The orientation vectors in Figure 3B  
 21 were generated using Orientation J.

22

## 23 **Particle Image Velocimetry**

1 4D data sets of NMY-2::GFP-expressing embryos were rotated relative to the angle of  
2 unilateral cleavage at 5% ring closure using an Image J function “3D projection.” We  
3 generated leading, lagging, and lateral cortex views based on the calculated ring closure  
4 angle. Note that not always both lagging and leading cortices were clearly visible, so that  
5 in some embryos, either leading or lagging cortex was used. Before executing “3D  
6 projection”, image planes equivalent to the near half-embryonic volume were deleted to  
7 avoid the visualization of the brighter cortical myosin at the opposite side. We also  
8 computationally deleted GFP::SAS-7 signals in the cytoplasm to avoid visualizing them  
9 after maximum projection. Using these flattened cell cortex images, Particle Image  
10 Velocimetry was performed using MATLAB software PIV LAB (Algorithm: FFT  
11 window deformation, Interrogation area: 5.8  $\mu\text{m}$ , Step size: 2.9  $\mu\text{m}$ , Sub-pixel estimator:  
12 Gauss 2x3 point, Correlation robustness: Standard) (Thielicke and Sonntag, 2021). We  
13 rejected vectors exceeding 0.25  $\mu\text{m}/\text{sec}$  to remove estimation errors (the setting was  
14 visually confirmed to reflect the myosin foci movement). Obtained 3D matrix data (2D x  
15 time) were used for the downstream analyses. The PIV matrix data were aligned relative  
16 to cytokinesis onset, centered relative to the cell center corresponding to the furrow  
17 position, and resized to contain an entire embryo using Numpy and Pandas (Harris et al.,  
18 2020; McKinney, 2010). Mean PIV vectors were calculated and plotted using Matplotlib  
19 (stream plot) (Hunter, 2007).

20

## 21 **Estimation of cortical convergence**

22 Cortical convergence was derived using the PIV vector matrix and a NumPy gradient  
23 function (Harris et al., 2020). When we define perpendicular-axis and ring-axis cortical

1 flow velocities in an  $i \times j$  matrix as  $u_{i,j}$  and  $v_{i,j}$ , respectively,  $u_{i+h,j}$ ,  $u_{i-h,j}$ ,  $v_{i,j+h}$ ,  $v_{i,j-h}$  can be  
2 defined as follows using Taylor series (Quarteroni et al., 2010):

$$3 \quad u_{i+h,j} = u_{i,j} + h \frac{\partial u_{i,j}}{\partial i} + \frac{h^2}{2!} \frac{\partial^2 u_{i,j}}{\partial i^2} + \mathcal{O}(h^3) \quad (4)$$

$$4 \quad u_{i-h,j} = u_{i,j} - h \frac{\partial u_{i,j}}{\partial i} + \frac{h^2}{2!} \frac{\partial^2 u_{i,j}}{\partial i^2} + \mathcal{O}(h^3) \quad (5)$$

$$5 \quad v_{i,j+h} = v_{i,j} + h \frac{\partial v_{i,j}}{\partial j} + \frac{h^2}{2!} \frac{\partial^2 v_{i,j}}{\partial j^2} + \mathcal{O}(h^3) \quad (6)$$

$$6 \quad v_{i,j-h} = v_{i,j} - h \frac{\partial v_{i,j}}{\partial j} + \frac{h^2}{2!} \frac{\partial^2 v_{i,j}}{\partial j^2} + \mathcal{O}(h^3) \quad (7)$$

7 And we will obtain the followings by subtraction:

$$8 \quad u_{i+h,j} - u_{i-h,j} = 2h \frac{\partial u_{i,j}}{\partial i} + \mathcal{O}(h^3) \quad (8)$$

$$9 \quad v_{i,j+h} - v_{i,j-h} = 2h \frac{\partial v_{i,j}}{\partial j} + \mathcal{O}(h^3) \quad (9)$$

10 Thus, the cortical flow gradients at the interior points can be defined as follows:

$$11 \quad \frac{\partial u_{i,j}}{\partial i} = \frac{u_{i+h,j} - u_{i-h,j}}{2h} + \mathcal{O}(h^2) \approx \frac{u_{i+h,j} - u_{i-h,j}}{2h} \quad (10)$$

$$12 \quad \frac{\partial v_{i,j}}{\partial j} = \frac{v_{i,j+h} - v_{i,j-h}}{2h} + \mathcal{O}(h^2) \approx \frac{v_{i,j+h} - v_{i,j-h}}{2h} \quad (11)$$

13 At the boundary, first order one-sided differences were achieved as follows:

$$14 \quad \frac{\partial u_{i,j}}{\partial i} = \frac{u_{i+h,j} - u_{i,j}}{h} + \mathcal{O}(h) \approx \frac{u_{i+h,j} - u_{i,j}}{h} \quad (12)$$

$$15 \quad \frac{\partial v_{i,j}}{\partial j} = \frac{v_{i,j+h} - v_{i,j}}{h} + \mathcal{O}(h) \approx \frac{v_{i,j+h} - v_{i,j}}{h} \quad (13)$$

16 Perpendicular-axis and ring-axis cortical convergence  $p_{i,j}$ ,  $q_{i,j}$ , respectively, were

17 calculated as follows, where  $a$  is the PIV step size:

$$p_{i,j} = -\frac{1}{a} \frac{\partial u_{i,j}}{\partial i} \approx -\frac{1}{a} \frac{(u_{i+1,j} - u_{i-1,j})}{2} \quad (\text{at the interior points}) \quad (14)$$

$$p_{i,j} = -\frac{1}{a} \frac{\partial u_{i,j}}{\partial i} \approx -\frac{1}{a} (u_{i\pm 1,j} - u_{i,j}) \quad (\text{at the boundary}) \quad (15)$$

$$q_{i,j} = -\frac{1}{a} \frac{\partial v_{i,j}}{\partial j} \approx -\frac{1}{a} \frac{(v_{i,j+1} - v_{i,j-1})}{2} \quad (\text{at the interior points}) \quad (16)$$

$$q_{i,j} = -\frac{1}{a} \frac{\partial v_{i,j}}{\partial j} \approx -\frac{1}{a} (v_{i,j\pm 1} - v_{i,j}) \quad (\text{at the boundary}) \quad (17)$$

Mean convergence of embryos was calculated for each grid, and plotted in Figure 4D using Matplotlib (stream plot). To quantify leading and lagging cortex convergence at the equatorial region in Figure 4E, we calculated mean convergence within a 6x3 grid (14.6  $\mu\text{m}$  W x 5.9  $\mu\text{m}$  H) around the center of the furrow position.

9

## 10 Myosin foci tracking

Before the analysis of myosin foci, cell position was registered using image J plug-in Stackreg, to eliminate the movement of myosin foci caused by the movement of cell body. Myosin foci in Figure 7B were tracked using Manual Tracking plug-in of Image J.

14

## 15 Statistical analysis

For multiple comparisons, one-way ANOVA with the Holm-Sidak's method was used. The comparison of two data was performed using the Mann-Whitney U-test or Welch's t-test. No statistical method was used to predetermine the sample size. Error bars or bands are corresponding to the 95% confidence interval. Pearson's coefficients were calculated in multiple 95 sec windows in Figure 5G. In Figure 5I, a 95 sec window corresponding to the ring oscillation period was used. The experiments were not randomized. The

1 investigators were not blinded to the study. Statistical analyses were performed using  
 2 either SciPy or Prism 9 (Graphpad). Symbols such as “\*\*\*\*”, “\*\*\*”, “\*\*”, and “\*”  
 3 indicate  $p < 0.0001$ ,  $p < 0.001$ ,  $p < 0.01$ , and  $p < 0.05$ , respectively.

4

5



# 1 **Figure legends**

2

## 3 **Figure 1. Intrinsic and extrinsic control of unilateral cytokinesis in *C. elegans***

4 **embryos.**

5 (A) Eccentric and concentric contractile ring closure of *C. elegans* embryonic  
6 blastomeres shown by volumetric 4D imaging of NMY-2::GFP (green, non-muscle  
7 myosin II), GFP::SAS-7 (green, centriole) and histone H2B::mCherry (magenta,  
8 chromosome) in the zygote P<sub>0</sub>, 2-cell stage AB, and isolated AB. In this and subsequent  
9 figures, anterior and posterior are to the left and right, respectively. (B) Trajectory of ring  
10 constriction. Outlines of the contractile ring during cytokinesis are plotted for single P<sub>0</sub>,  
11 AB, and isolated AB cells. Color coding indicates time relative to cytokinesis onset. (C)  
12 Mean ring closure and eccentricity. Times are relative to cytokinesis onset. Error bands  
13 indicate 95% confidence intervals. Scale bars, 10 μm.

14

## 15 **Figure 2. Mitotic spindle positioning, RhoA activity, and myosin enrichment are not** 16 **asymmetric at the beginning of the P<sub>0</sub> and AB cytokinesis.**

17 (A) Contractile ring assembly mechanism in *C. elegans* zygotes. (i) Mitotic spindle  
18 positioning determines the active RhoA zone where centralspindlin activates ECT-2-  
19 RhoGEF and RhoA; RhoA-GTP then activates myosin and actin assembly (“RhoA  
20 pathway”). (ii) At the cell surface, cortical flow compresses the equatorial cell cortex,  
21 producing actin alignment and myosin enrichment. Ring constriction further pulls the cell  
22 cortex to induce pole-to-equator cortical flow to form a positive feedback loop  
23 (“compression-feedback pathway”). (B, C) Centrosome positions relative to the axis of

1 contractile ring constriction. LE and LG indicate distances between the centrosome and  
2 cell cortex, respectively. **(D)** Kymographs of myosin and active RhoA localization at the  
3 equatorial cell cortex (ROI shown in B) using intensity-based color-coding. **(E)** Ratios of  
4 myosin and active RhoA signal intensities between leading and lagging cortices. Times  
5 are relative to cytokinesis onset. Error bands and bars indicate 95% confidence intervals.  
6 Scale bars, 10  $\mu$ m.

7

8 **Figure 3. Actin alignment asymmetry specifies leading and lagging cell cortices of P<sub>0</sub>**  
9 **cells.**

10 **(A)** F-actin distribution in leading and lagging cortices at 50 seconds before cytokinesis  
11 onset. White dotted boxes show F-actin alignments in B. Bottom panels show edge-  
12 enhanced images. **(B)** F-actin orientation at leading and lagging cell cortices. Yellow  
13 lines in the second and fourth columns indicate F-actin orientations. Each box is 12  $\times$  9  
14  $\mu$ m. **(C)** Circular means of F-actin orientation during P<sub>0</sub> cytokinesis. **(D)** Ratios of F-actin  
15 intensities between leading and lagging cortices. **(E)** Contractile ring trajectories after  
16 perturbation of key actin and myosin regulators. **(F)** Mean ring closures and  
17 eccentricities. Control data are the same as for Fig. 1C. **(G)** Eccentricities at 50% ring  
18 closure. Times are relative to cytokinesis onset. Error bands and bars indicate 95%  
19 confidence intervals. P-values were calculated using one-way ANOVA followed by  
20 Holm-Sidak's multiple comparison test. Scale bars, 10  $\mu$ m.

21

22 **Figure 4. Lagging equatorial cortex is compressed along the contractile ring axis in**  
23 **P<sub>0</sub> cells.**

(A) Cortical flow of a single embryo visualized from multiple angles. Yellow arrows indicate the movement of myosin foci from particle image velocimetry. (B, C) Concept of cortical convergence. Net influx and efflux of cortical flow within a certain area were calculated for the axes in parallel and perpendicular to the contractile ring (B). Cortical convergence indicates the degree of cortex compression before cleavage onset. After cleavage onset, convergence indicates both compression and the loss of cell surface from the focal plane due to invagination (C). (D) Mean cortical convergences and cortical flows calculated using the lateral cortex view. Arrow size scales with the cortical flow velocity. Convergence in the local area is shown by the color code. Dotted boxes indicate the equatorial regions of leading (top) and lagging (bottom) cortices. (E) Mean convergences calculated using leading and lagging cortex views. (F) Ring-axis convergences before cytokinesis onset. P-values were calculated by the Mann-Whitney U-test. Times are relative to cytokinesis onset. Error bands and bars indicate 95% confidence intervals. Scale bars, 10  $\mu$ m.

**Figure 5. Ring axis compression inhibits the furrow ingression and furrow-directed cortical flow.**

(A) Contractile ring trajectory of a single *act-2(or295ts)* mutant (left panel) and the average of ten embryos (graph). (B) Kymographs of the cortical NMY-2::GFP with intensity-based color coding. (C) Planes shown in (D-F). (D) NMY-2::GFP localization at the top surface during cytokinesis. Yellow and light blue dotted circles indicate the area exhibiting contraction and relaxation, respectively. (E) Ring en face view of the same embryo shown in panel D. Dotted lines indicate top and bottom limits of the

1 contractile ring. Arrows indicate the movement of the ring limit. (F) Ring trajectories of  
 2 the contractile ring shown in (E). Top- and bottom-oriented movements are shown in  
 3 yellow and blue, respectively. (G) Relationship between ring velocity and cortical  
 4 convergence. Ring centroid velocities of one embryo were plotted with ring axis  
 5 convergences at the top surface. Positive ring velocity represents ring ingression from the  
 6 top and vice versa. Pearson's correlation coefficients in 95 sec windows are also shown.  
 7 (H) Pearson's correlation coefficients between ring velocity and cortical convergence  
 8 from five embryos. (I) Furrow-directed movement of myosin clusters during relaxation.  
 9 Kymographs of individual and averaged clusters are shown relative to the time of peak  
 10 signal intensity. Except for I, times are relative to cytokinesis onset. Error bands indicate  
 11 95% confidence intervals. Scale bars, 10  $\mu$ m.

12

# 13 **Figure 6. Adhesion results in resistance of cleavage furrow ingression in AB cells.**

14 (A) Eccentric ring closure in AB cells. In addition to myosin II (green), cells are labeled  
 15 with centriole (green) and histone-H2B (magenta), except for *act-2(or295ts)* mutants.  
 16 White dotted lines indicate the AB-P<sub>1</sub> boundary. (B) Mean ring closure and eccentricity  
 17 in *pod-1(RNAi)*. (C) Ring eccentricity in intact embryos (control vs. *pod-1(RNAi)*), and in  
 18 isolated AB blastomeres with or without the attachment of adhesive beads. p-values were  
 19 calculated by Welch's t-test for the left graph and one-way ANOVA with Holm-Sidak's  
 20 multiple comparison test for the remaining data set. (D, E) Oblique view of contractile  
 21 rings in the bead attached AB cell. Ring trajectory and mean eccentricity are shown in D'  
 22 E' and D'' E'', respectively. (F) Ring eccentricity as a function of bead contact site. (G)  
 23 Angle of ingression during adhesion-dependent unilateral cleavage. Insets in the top

panels show the ring-bead interface. The graph at the right shows angles of ingression from three experiments. Times are relative to cytokinesis onset. Error bands and bars indicate 95% confidence intervals. Scale bars, 10  $\mu$ m.

4  
5

# **Figure 7. Adhesion inhibits furrow-directed cortical flow.**

(A) Isolated AB cells attached to adhesive beads of different diameters. (B) Furrow-directed cortical flow proximal (P) and distal (D) to bead attachment sites. (C) Myosin movement with a bead attached. Arrowheads indicate myosin foci. Arrows below micrographs indicate total displacements over 15 sec. (D) Working hypothesis for symmetry-breaking in unilateral cytokinesis. Ring-axis compression and cell-cell adhesion inhibit cortical ingression and furrow-directed cortical flow by suppressing ring-dependent cortex pulling (left diagram). Perpendicular-axis compression in wild-type embryos is a result of furrow-directed cortical flow that induces myosin enrichment at the equatorial cortex through compression-dependent feedback. Suppression of cell cortex pulling induces unilateral cytokinesis with and without the compression-dependent feedback. Cortical stiffness asymmetry induced by intrinsic cortical dynamics and external adhesion is the symmetry-breaking cue (right diagram). Differences in ring trajectories can be explained by differences in the timing of stiffness change (diagrams i-iv, lower right panel). Error bars indicate 95% confidence intervals. Scale bars, 10  $\mu$ m. p-values were calculated by one-way ANOVA with Holm-Sidak's multiple comparison test.

23

# **Figure S1. Imaging and contractile ring analysis methods.**

(A) Imaging conditions and analytical flow charts. For intact embryos, we used refractive index matching medium and polystyrene beads as spacers. For isolated AB blastomeres, we used a normal growth medium and a different analytical pipeline to estimate ring size and position because of the cells' movement and rotation. Isolated AB cells were measured three times, and average values were analyzed. (B) Temporal color-coded image of 20 frames around cytokinesis onset showing that compression-free embryos do not exhibit global cortical rotation. (C) Ring en face view after the rotation of 3D projected data and ring segmentation. (D) Contractile ring closure data after alignment of time series data relative to 2 % ring closure. Error bars indicate 95% confidence intervals.

# **Figure S2. Comparison between our methods and those of Khaliulin et al. (2018).**

(A) Left, a previous study by Khaliulin et al. used 0.5% thick agarose to mitigate compression, while our method does so using beads. Our data have increased spatial-temporal information regarding ring dynamics, while our axial and temporal resolution of cortical flow is lower. Nevertheless, the perpendicular-axis cortical flow data are highly reproducible and in good agreement with those of Khaliulin et al. (B) Left, Khaliulin et al. aligned data using a line passing through the 30% and 80% ring closure points. By linear extrapolation of the line to 100 and 0, tck and t0 were defined (red line). According to the paper, t0 and tck corresponded to 10% and 90% ring closure, respectively. Right, in our study, we aligned time-series data relative to 2% ring closure point to focus on earlier symmetry-breaking events. Using the method used by Khaliulin et al., t0 and tck in our data set are nearly identical at 11% and 94%, respectively. The time range of data

1 reported by Khaliulin et al. was -0.25 t/tck to 1.0 t/tck (= tck), which is between 6.25 sec  
2 and 240 sec after cytokinesis onset based on our estimation. On the other hand, our data  
3 also includes 50–80 sec before cytokinesis onset.

4

### 5 **Figure S3. Measurement of centrosome positioning and signal intensity.**

6 (A) Image analysis pipelines for P0 (left) and AB (right) spindle positioning. All  
7 processes were performed semi-automatically using in-house image J macros. (B) Image  
8 analysis pipeline for active RhoA and myosin signal intensities. White boxes in the insets  
9 of images on the right show the areas of measurement.

10

### 11 **Movie S1. Dynamics of cortical myosin and contractile ring of a single embryo**

12 Left top: maximum projection of cell surface NMY-2::GFP. Bottom left: ring en face  
13 view of NMY-2::GFP. Bottom middle: segmented ring. Bottom right: reconstructed ring  
14 trajectory. Right graph: Contractile ring dynamics of the same embryo. Note that an  
15 identical embryo was used to generate all data.

16

### 17 **Movie S2. Cortical flow and flow vector map using Particle Image Velocimetry**

18 The cell surface NMY-2::GFP of leading (left), lateral (middle), and lagging cortex views  
19 (right). Yellow arrows are generated by Particle Image Velocimetry. Times are relative to  
20 cytokinesis onset.

21

### 22 **Movie S3. Average cortical flow and convergence map using lateral view**

1 Perpendicular-axis (left) and ring-axis convergences (right) are shown. The color code is  
 2 the same as Figure 4D (warm color: positive, cool color: negative values). Times are  
 3 relative to cytokinesis onset.

4

# 5 **Movie S4. Dynamics of cortical compression and cortical ingression**

6 Cell surface (top) and ring en face view (bottom left) of NMY-2::GFP. Ring outlines and  
 7 centroid trajectory were color coded as in Figure 5F (yellow: movement towards the  
 8 contraction site, blue color: movement away from the relaxation site).

9

10

11

12

13

14

15

16



# References

- Ahringer, J. (2006). Reverse genetics. WormBook  
<https://doi.org/10.1895/wormbook.1.47.1>.
- Basant, A., and Glotzer, M. (2018). Spatiotemporal Regulation of RhoA during Cytokinesis. *Curr. Biol.* 28, R570–R580. .
- Basant, A., Lekomtsev, S., Tse, Y.C., Zhang, D., Longhini, K.M., Petronczki, M., and Glotzer, M. (2015). Aurora B kinase promotes cytokinesis by inducing centralspindlin oligomers that associate with the plasma membrane. *Dev. Cell* 33, 204–215. .
- Bement, W.M., Benink, H.A., and von Dassow, G. (2005). A microtubule-dependent zone of active RhoA during cleavage plane specification. *J. Cell Biol.* 170, 91–101. .
- Biot, E., Crowell, E., Hofte, H., Maurin, Y., Vernhettes, S., and Andrey, P. (2008). A new filter for spot extraction in n-dimensional biological imaging. In 2008 5th IEEE International Symposium on Biomedical Imaging: From Nano to Macro, pp. 975–978.
- Bourdages, K.G., Lacroix, B., Dorn, J.F., Descovich, C.P., and Maddox, A.S. (2014). Quantitative analysis of cytokinesis in situ during *C. elegans* postembryonic development. *PLoS One* 9, e110689. .
- Bray, D., and White, J.G. (1988). Cortical flow in animal cells. *Science* 239, 883–888. .
- Brenner, S. (1974). The genetics of *Caenorhabditis elegans*. *Genetics* 77, 71–94. .
- Chan, F.-Y., Silva, A.M., Saramago, J., Pereira-Sousa, J., Brighton, H.E., Pereira, M., Oegema, K., Gassmann, R., and Carvalho, A.X. (2019). The ARP2/3 complex prevents excessive formin activity during cytokinesis. *Mol. Biol. Cell* 30, 96–107. .
- Chapa-Y-Lazo, B., Hamanaka, M., Wray, A., Balasubramanian, M.K., and Mishima, M. (2020). Polar relaxation by dynein-mediated removal of cortical myosin II. *J. Cell Biol.* 219. <https://doi.org/10.1083/jcb.201903080>.
- Douglas, M.E., Davies, T., Joseph, N., and Mishima, M. (2010). Aurora B and 14-3-3 coordinately regulate clustering of centralspindlin during cytokinesis. *Curr. Biol.* 20, 927–933. .
- Fleming, E.S., Zajac, M., Moschenross, D.M., Montrose, D.C., Rosenberg, D.W., Cowan, A.E., and Tirnauer, J.S. (2007). Planar spindle orientation and asymmetric cytokinesis in the mouse small intestine. *J. Histochem. Cytochem.* 55, 1173–1180. .
- Founounou, N., Loyer, N., and Le Borgne, R. (2013). Septins regulate the contractility of the actomyosin ring to enable adherens junction remodeling during cytokinesis of epithelial cells. *Dev. Cell* 24, 242–255. .

- 1 Goley, E.D., and Welch, M.D. (2006). The ARP2/3 complex: an actin nucleator comes of  
2 age. *Nat. Rev. Mol. Cell Biol.* 7, 713–726. .
- 3 Gómez-Cavazos, J.S., Lee, K.-Y., Lara-González, P., Li, Y., Desai, A., Shiau, A.K., and  
4 Oegema, K. (2020). A Non-canonical BRCT-Phosphopeptide Recognition Mechanism  
5 Underlies RhoA Activation in Cytokinesis. *Curr. Biol.* 30, 3101-3115.e11. .
- 6 Greenspan, H.P. (1978). On fluid-mechanical simulations of cell division and movement.  
7 *J. Theor. Biol.* 70, 125–134. .
- 8 Guillot, C., and Lecuit, T. (2013). Adhesion disengagement uncouples intrinsic and  
9 extrinsic forces to drive cytokinesis in epithelial tissues. *Dev. Cell* 24, 227–241. .
- 10 Harris, C.R., Millman, K.J., van der Walt, S.J., Gommers, R., Virtanen, P., Cournapeau,  
11 D., Wieser, E., Taylor, J., Berg, S., Smith, N.J., et al. (2020). Array programming with  
12 NumPy. *Nature* 585, 357–362. .
- 13 Herszterg, S., Leibfried, A., Bosveld, F., Martin, C., and Bellaiche, Y. (2013). Interplay  
14 between the Dividing Cell and Its Neighbors Regulates Adherens Junction Formation  
15 during Cytokinesis in Epithelial Tissue. *Dev. Cell* 24, 256–270. .
- 16 Hsu, C.R., Xiong, R., and Sugioka, K. (2019). In Vitro Reconstitution of Spatial Cell  
17 Contact Patterns with Isolated *Caenorhabditis elegans* Embryo Blastomeres and Adhesive  
18 Polystyrene Beads. *J. Vis. Exp.* <https://doi.org/10.3791/60422>.
- 19 Hunter, J.D. (2007). Matplotlib: A 2D Graphics Environment. *Comput. Sci. Eng.* 9, 90–  
20 95. .
- 21 Khaliullin, R.N., Green, R.A., Shi, L.Z., Gomez-Cavazos, J.S., Berns, M.W., Desai, A.,  
22 and Oegema, K. (2018). A positive-feedback-based mechanism for constriction rate  
23 acceleration during cytokinesis in *Caenorhabditis elegans*. *Elife* 7.  
24 <https://doi.org/10.7554/elife.36073>.
- 25 Koyama, H., Umeda, T., Nakamura, K., Higuchi, T., and Kimura, A. (2012). A high-  
26 resolution shape fitting and simulation demonstrated equatorial cell surface softening  
27 during cytokinesis and its promotive role in cytokinesis. *PLoS One* 7, e31607. .
- 28 Legland, D., Arganda-Carreras, I., and Andrey, P. (2016). MorphoLibJ: integrated library  
29 and plugins for mathematical morphology with ImageJ. *Bioinformatics* 32, 3532–3534. .
- 30 Li, Y., and Munro, E. (2021). Filament-guided filament assembly provides structural  
31 memory of filament alignment during cytokinesis. *Dev. Cell* 56, 2486-2500.e6. .
- 32 Liu, J., Fairn, G.D., Ceccarelli, D.F., Sicheri, F., and Wilde, A. (2012). Cleavage Furrow  
33 Organization Requires PIP2-Mediated Recruitment of Anillin. *Curr. Biol.* 22, 64–69. .
- 34 Maddox, A.S., Lewellyn, L., Desai, A., and Oegema, K. (2007). Anillin and the septins  
35 promote asymmetric ingression of the cytokinetic furrow. *Dev. Cell* 12, 827–835. .

- 1 Matsumura, F. (2005). Regulation of myosin II during cytokinesis in higher eukaryotes.  
2 Trends Cell Biol. 15, 371–377. .
- 3 McKinney, W. (2010). Data Structures for Statistical Computing in Python. In  
4 Proceedings of the 9th Python in Science Conference, (SciPy), p.
- 5 Meijering, E. Feature J: An Image J Plugin Suite for Image Feature Extraction.
- 6 Morais-de-Sá, E., and Sunkel, C. (2013). Adherens junctions determine the apical  
7 position of the midbody during follicular epithelial cell division. EMBO Rep. 14, 696–  
8 703. .
- 9 Nakajima, Y.-I., Lee, Z.T., McKinney, S.A., Swanson, S.K., Florens, L., and Gibson,  
10 M.C. (2019). Junctional tumor suppressors interact with 14-3-3 proteins to control planar  
11 spindle alignment. J. Cell Biol. 218, 1824–1838. .
- 12 van Oostende Triplet, C., Jaramillo Garcia, M., Haji Bik, H., Beaudet, D., and Piekny, A.  
13 (2014). Anillin interacts with microtubules and is part of the astral pathway that defines  
14 cortical domains. J. Cell Sci. 127, 3699–3710. .
- 15 Otomo, T., Otomo, C., Tomchick, D.R., Machius, M., and Rosen, M.K. (2005).  
16 Structural basis of Rho GTPase-mediated activation of the formin mDia1. Mol. Cell 18,  
17 273–281. .
- 18 Ozugergin, I., Mastronardi, K., Law, C., and Piekny, A. (2022). Diverse mechanisms  
19 regulate contractile ring assembly for cytokinesis in the two-cell Caenorhabditis elegans  
20 embryo. J. Cell Sci. 135. <https://doi.org/10.1242/jcs.258921>.
- 21 Piekny, A.J., and Glotzer, M. (2008). Anillin is a scaffold protein that links RhoA, actin,  
22 and myosin during cytokinesis. Curr. Biol. 18, 30–36. .
- 23 Püspöki, Z., Storath, M., Sage, D., and Unser, M. (2016). Transforms and Operators for  
24 Directional Bioimage Analysis: A Survey. Adv. Anat. Embryol. Cell Biol. 219, 69–93. .
- 25 Quarteroni, A., Sacco, R., and Saleri, F. (2010). Numerical Mathematics (Springer  
26 Science & Business Media).
- 27 Rappaport, R. (1986). Establishment of the Mechanism of Cytokinesis in Animal Cells.  
28 In International Review of Cytology, G.H. Bourne, K.W. Jeon, and M. Friedlander, eds.  
29 (Academic Press), pp. 245–281.
- 30 Rappaport, R. (1996). Division Mechanism Function and Its Consequences. In  
31 Cytokinesis in Animal Cells, (Cambridge University Press), pp. 230–264.
- 32 Rappaport, R., and Conrad, G.W. (1963). AN EXPERIMENTAL ANALYSIS OF  
33 UNILATERAL CLEAVAGE IN INVERTEBRATE EGGS. J. Exp. Zool. 153, 99–112. .

- 1 Reymann, A.-C., Staniscia, F., Erzberger, A., Salbreux, G., and Grill, S.W. (2016).
- 2 Cortical flow aligns actin filaments to form a furrow. *Elife* 5, e17807. .
- 3 Royer, L.A., Weigert, M., Günther, U., Maghelli, N., Jug, F., Sbalzarini, I.F., and Myers,
- 4 E.W. (2015). ClearVolume: open-source live 3D visualization for light-sheet microscopy.
- 5 *Nat. Methods* 12, 480–481. .
- 6 Schindelin, J., Arganda-Carreras, I., Frise, E., Kaynig, V., Longair, M., Pietzsch, T.,
- 7 Preibisch, S., Rueden, C., Saalfeld, S., Schmid, B., et al. (2012). Fiji: an open-source
- 8 platform for biological-image analysis. *Nat. Methods* 9, 676–682. .
- 9 Schonegg, S., Hyman, A.A., and Wood, W.B. (2014). Timing and mechanism of the
- 10 initial cue establishing handed left–right asymmetry in *Caenorhabditis elegans* embryos.
- 11 *Genesis* 52, 572–580. .
- 12 Shelton, C.A., and Bowerman, B. (1996). Time-dependent responses to glp-1-mediated
- 13 inductions in early *C. elegans* embryos. *Development* 122, 2043–2050. .
- 14 Singh, D., Odedra, D., Dutta, P., and Pohl, C. (2019). Mechanical stress induces a
- 15 scalable switch in cortical flow polarization during cytokinesis. *J. Cell Sci.* 132.
- 16 <https://doi.org/10.1242/jcs.231357>.
- 17 Somers, W.G., and Saint, R. (2003). A RhoGEF and Rho family GTPase-activating
- 18 protein complex links the contractile ring to cortical microtubules at the onset of
- 19 cytokinesis. *Dev. Cell* 4, 29–39. .
- 20 Sugioka, K. (2021). Symmetry-breaking of animal cytokinesis. *Semin. Cell Dev. Biol.*
- 21 <https://doi.org/10.1016/j.semcdb.2021.12.008>.
- 22 Sugioka, K., and Bowerman, B. (2018). Combinatorial Contact Cues Specify Cell
- 23 Division Orientation by Directing Cortical Myosin Flows. *Dev. Cell* 46, 257-270.e5. .
- 24 Tatsumoto, T., Xie, X., Blumenthal, R., Okamoto, I., and Miki, T. (1999). Human ECT2
- 25 is an exchange factor for Rho GTPases, phosphorylated in G2/M phases, and involved in
- 26 cytokinesis. *J. Cell Biol.* 147, 921–928. .
- 27 Taulet, N., Vitre, B., Anguille, C., Douanier, A., Rocancourt, M., Taschner, M.,
- 28 Lorentzen, E., Echard, A., and Delaval, B. (2017). IFT proteins spatially control the
- 29 geometry of cleavage furrow ingression and lumen positioning. *Nat. Commun.* 8, 1928. .
- 30 Thévenaz, P., Ruttimann, U.E., and Unser, M. (1998). A pyramid approach to subpixel
- 31 registration based on intensity. *IEEE Trans. Image Process.* 7, 27–41. .
- 32 Thieleke-Matos, C., Osório, D.S., Carvalho, A.X., and Morais-de-Sá, E. (2017).
- 33 Emerging Mechanisms and Roles for Asymmetric Cytokinesis. *Int. Rev. Cell Mol. Biol.*
- 34 332, 297–345. .

- 1 Thielicke, W., and Sonntag, R. (2021). Particle Image Velocimetry for MATLAB:  
2 Accuracy and enhanced algorithms in PIVlab. *J. Open Res. Softw.* *9*, 12. .
- 3 Tse, Y.C., Werner, M., Longhini, K.M., Labbe, J.-C., Goldstein, B., and Glotzer, M.  
4 (2012). RhoA activation during polarization and cytokinesis of the early *Caenorhabditis*  
5 *elegans* embryo is differentially dependent on NOP-1 and CYK-4. *Mol. Biol. Cell* *23*,  
6 4020–4031. .
- 7 Virtanen, P., Gommers, R., Oliphant, T.E., Haberland, M., Reddy, T., Cournapeau, D.,  
8 Burovski, E., Peterson, P., Weckesser, W., Bright, J., et al. (2020). SciPy 1.0:  
9 fundamental algorithms for scientific computing in Python. *Nat. Methods* *17*, 261–272. .
- 10 Willis, J.H., Munro, E., Lyczak, R., and Bowerman, B. (2006). Conditional dominant  
11 mutations in the *Caenorhabditis elegans* gene *act-2* identify cytoplasmic and muscle roles  
12 for a redundant actin isoform. *Mol. Biol. Cell* *17*, 1051–1064. .
- 13 Wolpert, L. (1960). The mechanics and mechanism of cleavage. *Int. Rev. Cytol.* *10*, 163–  
14 216. .
- 15 Woolner, S., and Papalopulu, N. (2012). Spindle position in symmetric cell divisions  
16 during epiboly is controlled by opposing and dynamic apicobasal forces. *Dev. Cell* *22*,  
17 775–787. .
- 18 Xie, C., Jiang, Y., Zhu, Z., Huang, S., Li, W., and Ou, G. (2021). Actin filament  
19 debranching regulates cell polarity during cell migration and asymmetric cell division.  
20 *Proc. Natl. Acad. Sci. U. S. A.* *118*. <https://doi.org/10.1073/pnas.2100805118>.
- 21 Xiong, R., and Sugioka, K. (2020). Improved 3D cellular morphometry of *Caenorhabditis*  
22 *elegans* embryos using a refractive index matching medium. *PLoS One* *15*, e0238955. .
- 23 Yatsu, N. (1912). Observations and experiments on the ctenophore egg. *Jour. Coll. Sci.*  
24 *Tokyo* *32*, 1–21. .
- 25 Yüce, O., Piekny, A., and Glotzer, M. (2005). An ECT2-centralspindlin complex  
26 regulates the localization and function of RhoA. *J. Cell Biol.* *170*, 571–582. .
- 27 Zinemanas, D., and Nir, A. (1987). Fluid Mechanical Simulations of Cell Furrowing Due  
28 to Anisotropic Surface Forces. In *Biomechanics of Cell Division*, N. Akkas, ed. (Boston,  
29 MA: Springer US), pp. 281–305.
- 30 Zinemanas, D., and Nir, A. (1988). On the viscous deformation of biological cells under  
31 anisotropic surface tension. *J. Fluid Mech.* *193*, 217–241. .



# Figure 1 (Hsu, Sangha, Fan, et al.)

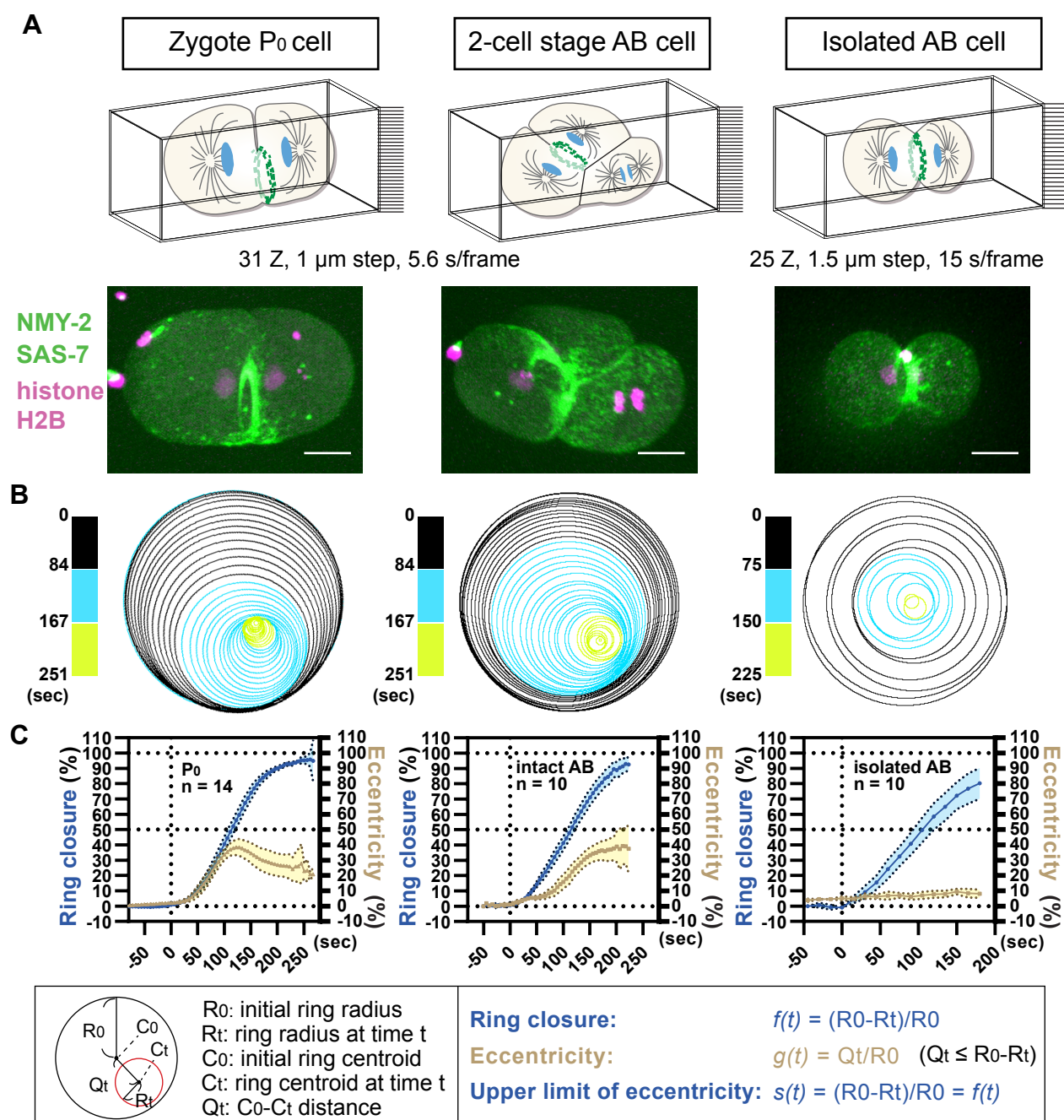


**Figure 1. Intrinsic and extrinsic control of unilateral cytokinesis in *C. elegans* embryos.**

(A) Eccentric and concentric contractile ring closure of *C. elegans* embryonic blastomeres shown by volumetric 4D imaging of NMY-2::GFP (green, non-muscle myosin II), GFP::SAS-7 (green, centriole) and histone H2B::mCherry (magenta, chromosome) in the zygote P<sub>0</sub>, 2-cell stage AB, and isolated AB. In this and subsequent figures, anterior and posterior are to the left and right, respectively. (B) Trajectory of ring constriction. Outlines of the contractile ring during cytokinesis are plotted for single P<sub>0</sub>, AB, and isolated AB cells. Color coding indicates time relative to cytokinesis onset. (C) Mean ring closure and eccentricity. Times are relative to cytokinesis onset. Error bands indicate 95% confidence intervals. Scale bars, 10 μm.

## Figure 2 (Hsu, Sangha, Fan, et al.)

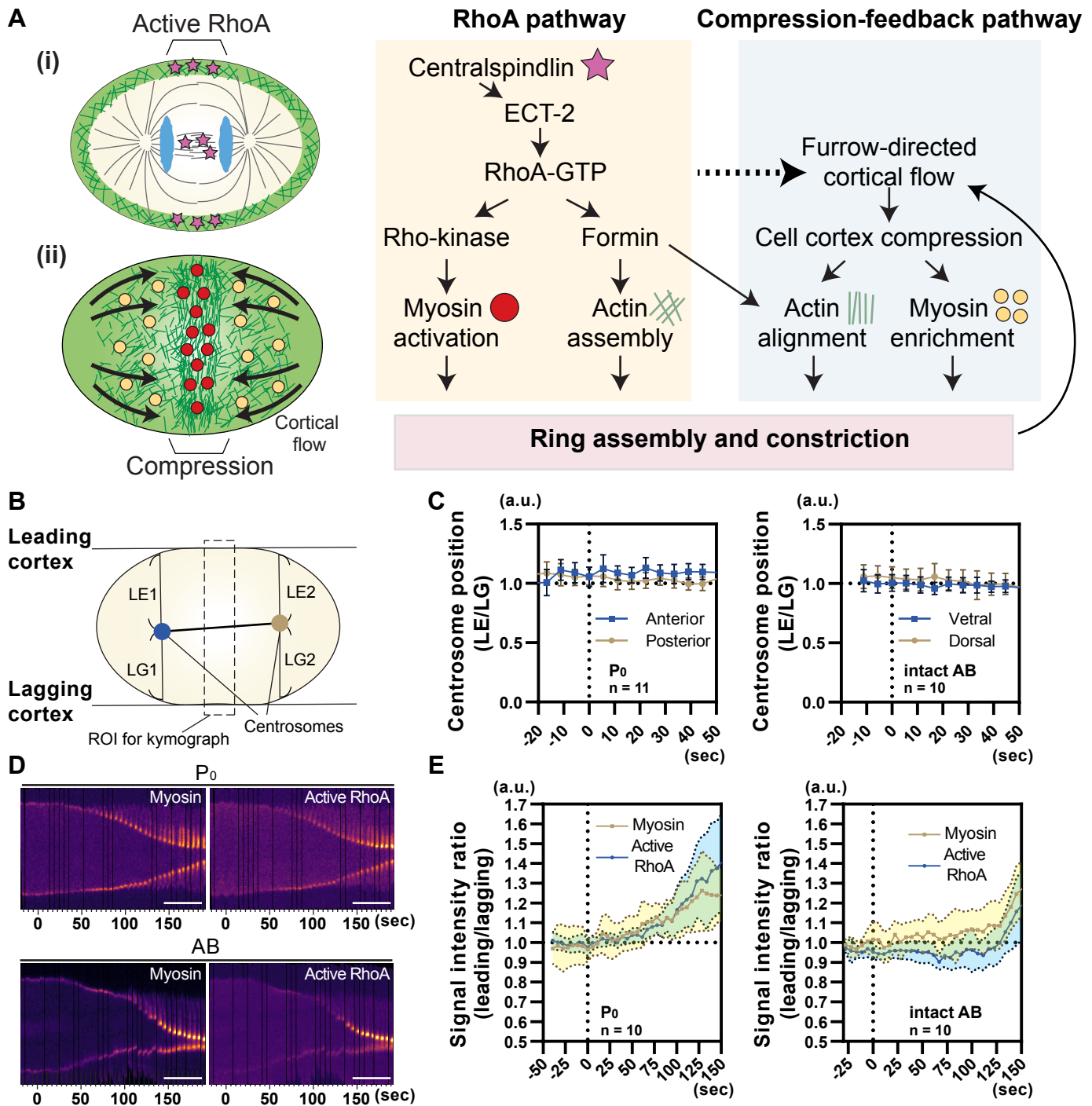


**Figure 2. Mitotic spindle positioning, RhoA activity, and myosin enrichment are not asymmetric at the beginning of the  $P_0$  and AB cytokinesis.**

(A) Contractile ring assembly mechanism in *C. elegans* zygotes. (i) Mitotic spindle positioning determines the active RhoA zone where centralspindlin activates ECT-2-RhoGEF and RhoA; RhoA-GTP then activates myosin and actin assembly ("RhoA pathway"). (ii) At the cell surface, cortical flow compresses the equatorial cell cortex, producing actin alignment and myosin enrichment. Ring constriction further pulls the cell cortex to induce pole-to-equator cortical flow to form a positive feedback loop ("compression-feedback pathway"). (B, C) Centrosome positions relative to the axis of contractile ring constriction. LE and LG indicate distances between the centrosome and cell cortex, respectively. (D) Kymographs of myosin and active RhoA localization at the equatorial cell cortex (ROI shown in B) using intensity-based color-coding. (E) Ratios of myosin and active RhoA signal intensities between leading and lagging cortices. Times are relative to cytokinesis onset. Error bands and bars indicate 95% confidence intervals. Scale bars, 10  $\mu$ m.



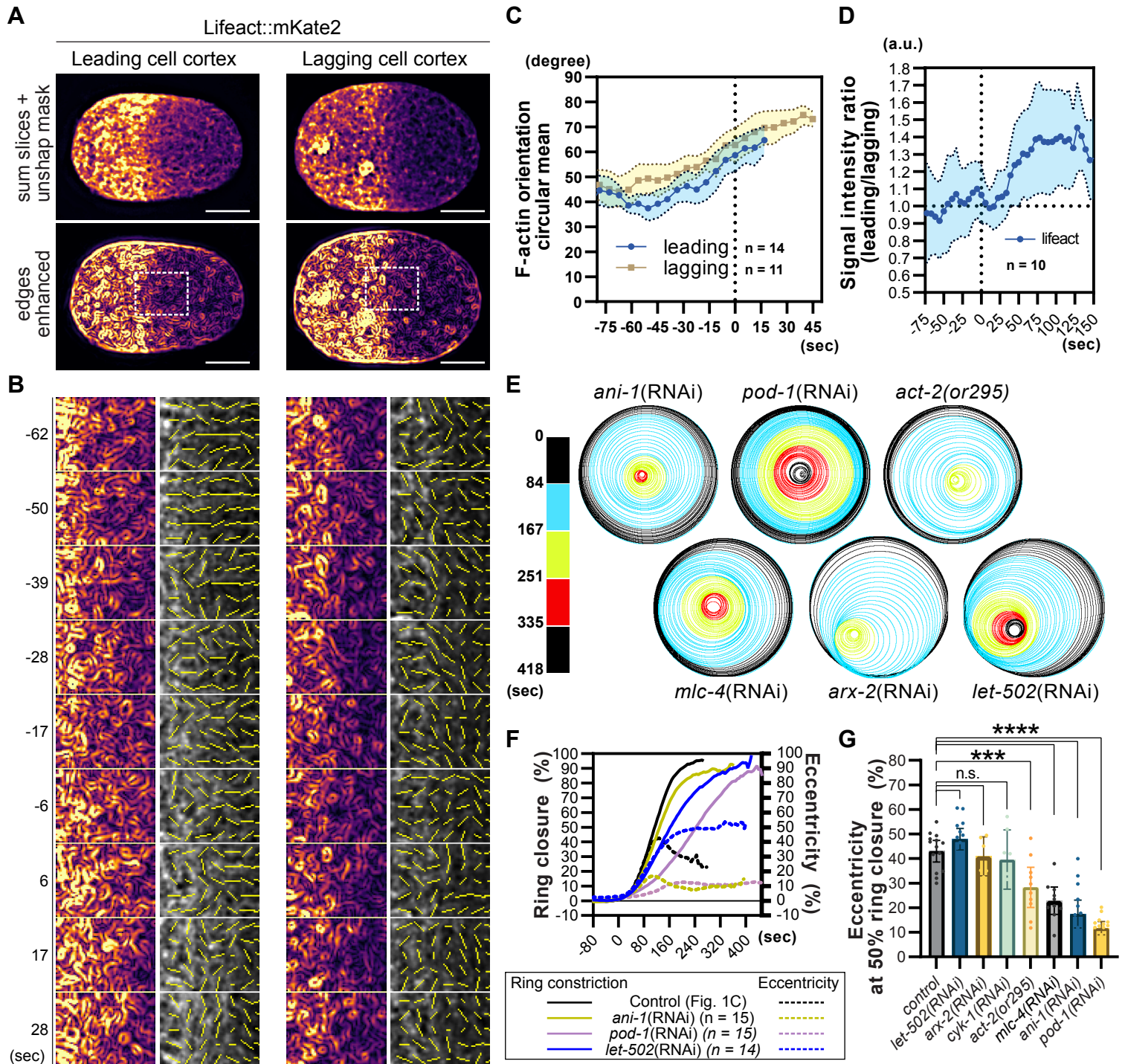


**Figure 3. Actin alignment asymmetry specifies leading and lagging cell cortices of P0 cells.**

(A) F-actin distribution in leading and lagging cortices at 50 seconds before cytokinesis onset. White dotted boxes show F-actin alignments in B. Bottom panels show edge-enhanced images. (B) F-actin orientation at leading and lagging cell cortices. Yellow lines in the second and fourth columns indicate F-actin orientations. Each box is  $12 \times 9 \mu\text{m}$ . (C) Circular means of F-actin orientation during P0 cytokinesis. (D) Ratios of F-actin intensities between leading and lagging cortices. (E) Contractile ring trajectories after perturbation of key actin and myosin regulators. (F) Mean ring closures and eccentricities. Control data are the same as for Fig. 1C. (G) Eccentricities at 50% ring closure. Times are relative to cytokinesis onset. Error bands and bars indicate 95% confidence intervals. P-values were calculated using one-way ANOVA followed by Holm-Sidak's multiple comparison test. Scale bars,  $10 \mu\text{m}$ .



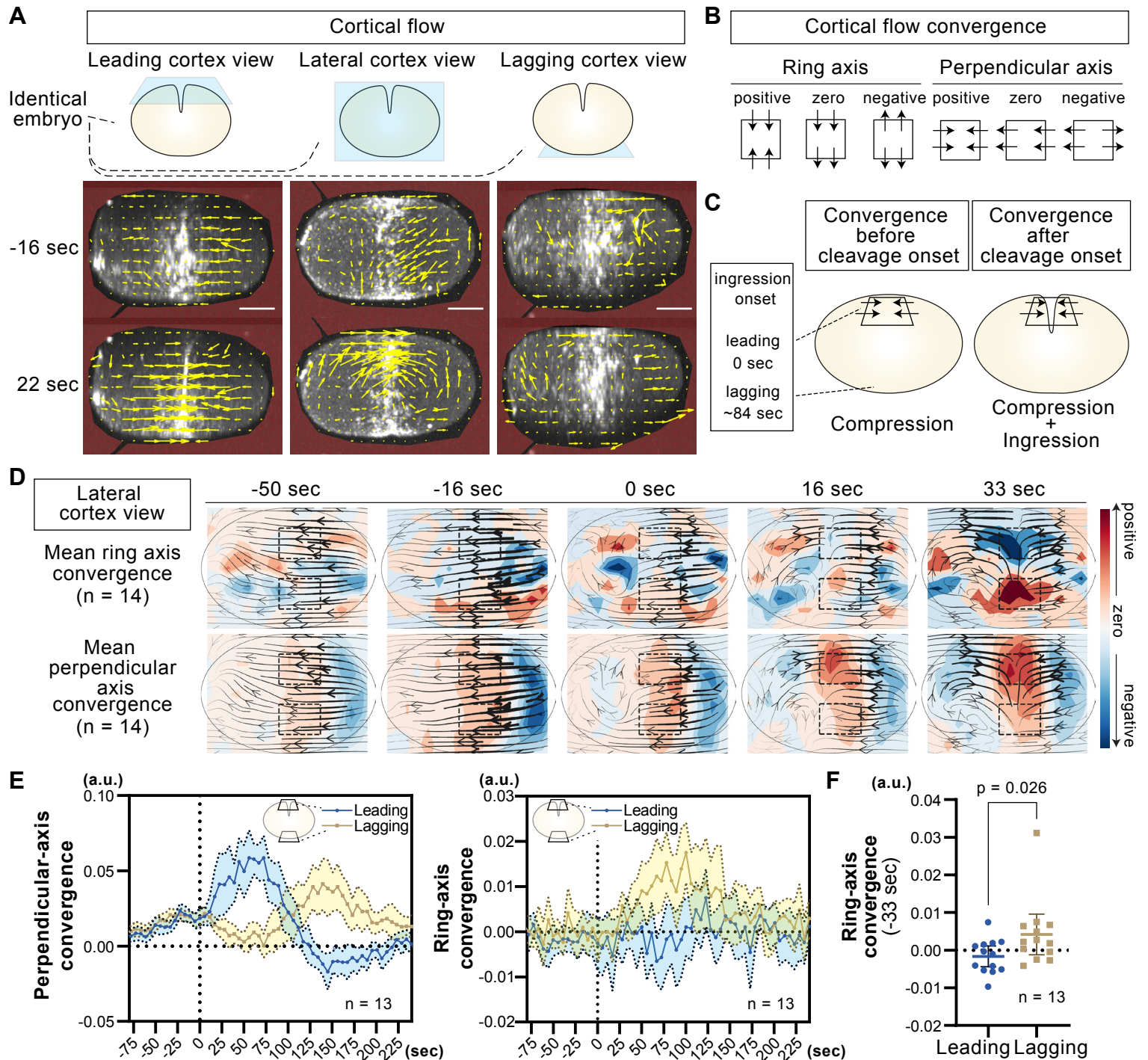


**Figure 4. Lagging equatorial cortex is compressed along the contractile ring axis in P0 cells.**

(A) Cortical flow of a single embryo visualized from multiple angles. Yellow arrows indicate the movement of myosin foci from particle image velocimetry. (B, C) Concept of cortical convergence. Net influx and efflux of cortical flow within a certain area were calculated for the axes in parallel and perpendicular to the contractile ring (B). Cortical convergence indicates the degree of cortex compression before cleavage onset. After cleavage onset, convergence indicates both compression and the loss of cell surface from the focal plane due to invagination (C). (D) Mean cortical convergences and cortical flows calculated using the lateral cortex view. Arrow size scales with the cortical flow velocity. Convergence in the local area is shown by the color code. Dotted boxes indicate the equatorial regions of leading (top) and lagging (bottom) cortices. (E) Mean convergences calculated using leading and lagging cortex views. (F) Ring-axis convergences before cytokinesis onset. P-values were calculated by the Mann-Whitney U-test. Times are relative to cytokinesis onset. Error bands and bars indicate 95% confidence intervals. Scale bars, 10  $\mu$ m.

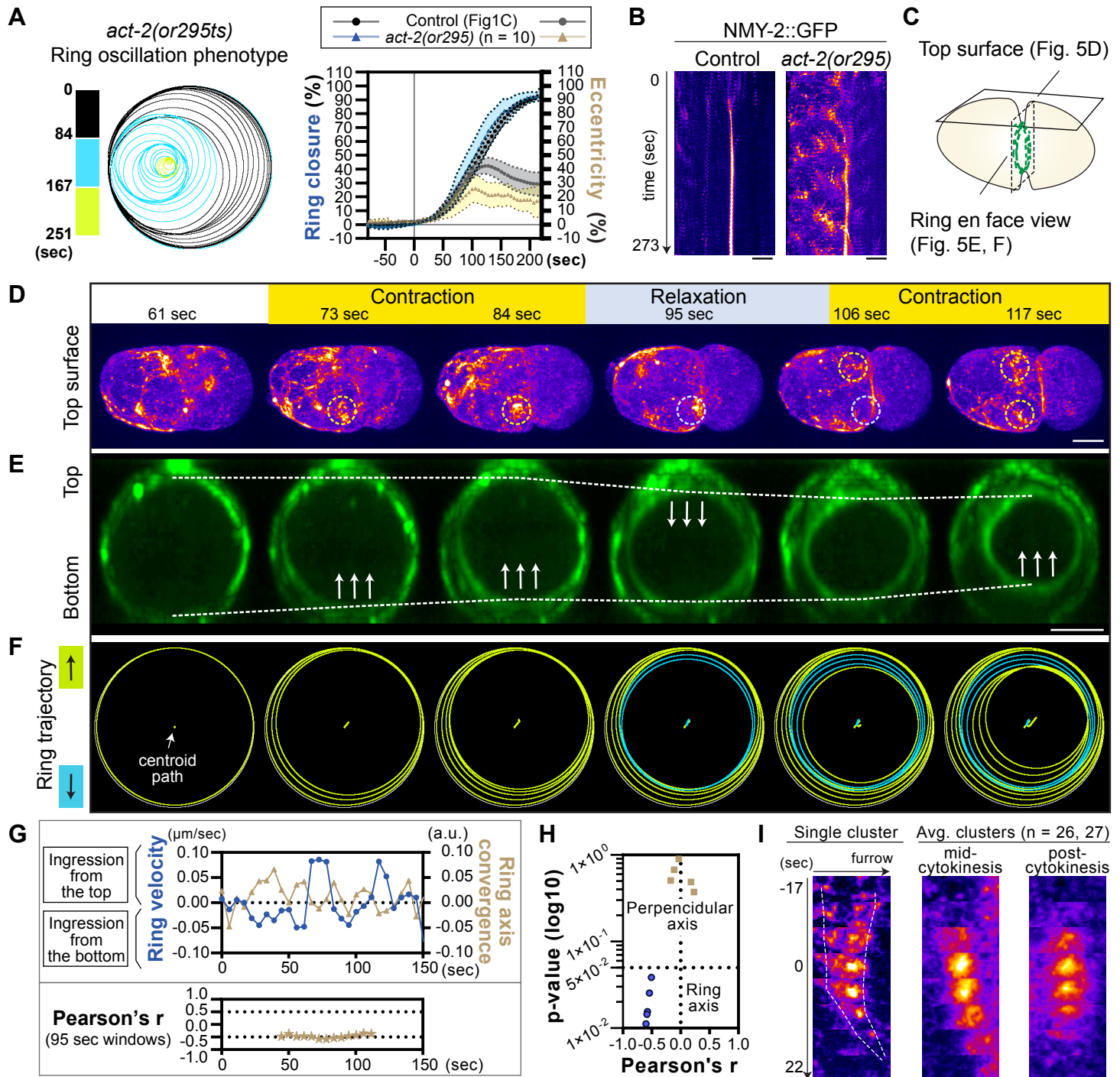


**Figure 5. Ring axis compression inhibits the furrow ingression and furrow-directed cortical flow.**

(A) Contractile ring trajectory of a single *act-2(or295ts)* mutant (left panel) and the average of ten embryos (graph). (B) Kymographs of the cortical NMY-2::GFP with intensity-based color coding. (C) Planes shown in (D-F). (D) NMY-2::GFP localization at the top surface during cytokinesis. Yellow and light blue dotted circles indicate the area exhibiting contraction and relaxation, respectively. (E) Ring en face view of the same embryo shown in panel D. Dotted lines indicate top and bottom limits of the contractile ring. Arrows indicate the movement of the ring limit. (F) Ring trajectories of the contractile ring shown in (E). Top- and bottom-oriented movements are shown in yellow and blue, respectively. (G) Relationship between ring velocity and cortical convergence. Ring centroid velocities of one embryo were plotted with ring axis convergences at the top surface. Positive ring velocity represents ring ingression from the top and vice versa. Pearson's correlation coefficients in 95 sec windows are also shown. (H) Pearson's correlation coefficients between ring velocity and cortical convergence from five embryos. (I) Furrow-directed movement of myosin clusters during relaxation. Kymographs of individual and averaged clusters are shown relative to the time of peak signal intensity. Except for I, times are relative to cytokinesis onset. Error bands indicate 95% confidence intervals. Scale bars, 10 μm.



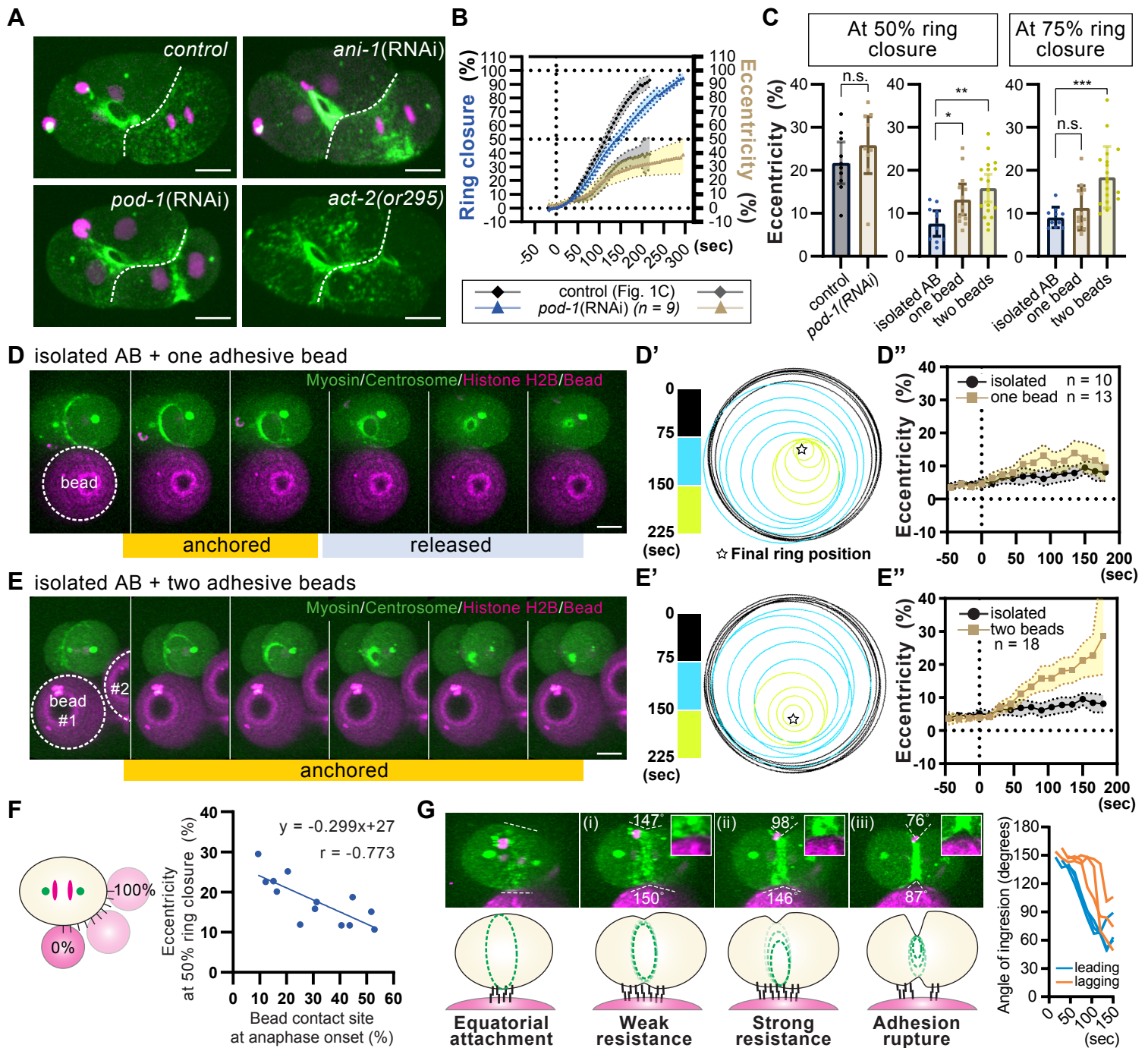


**Figure 6. Adhesion results in resistance of cleavage furrow ingression in AB cells.**

(A) Eccentric ring closure in AB cells. In addition to myosin II (green), cells are labeled with centriole (green) and histone-H2B (magenta), except for *act-2(or295ts)* mutants. White dotted lines indicate the AB-P1 boundary. (B) Mean ring closure and eccentricity in *pod-1(RNAi)*. (C) Ring eccentricity in intact embryos (control vs. *pod-1(RNAi)*), and in isolated AB blastomeres with or without the attachment of adhesive beads. p-values were calculated by Welch's t-test for the left graph and one-way ANOVA with Holm-Sidak's multiple comparison test for the remaining data set. (D, E) Oblique view of contractile rings in the bead attached AB cell. Ring trajectory and mean eccentricity are shown in D' E' and D'' E'', respectively. (F) Ring eccentricity as a function of bead contact site. (G) Angle of ingression during adhesion-dependent unilateral cleavage. Insets in the top panels show the ring-bead interface. The graph at the right shows angles of ingression from three experiments. Times are relative to cytokinesis onset. Error bands and bars indicate 95% confidence intervals. Scale bars, 10  $\mu$ m.

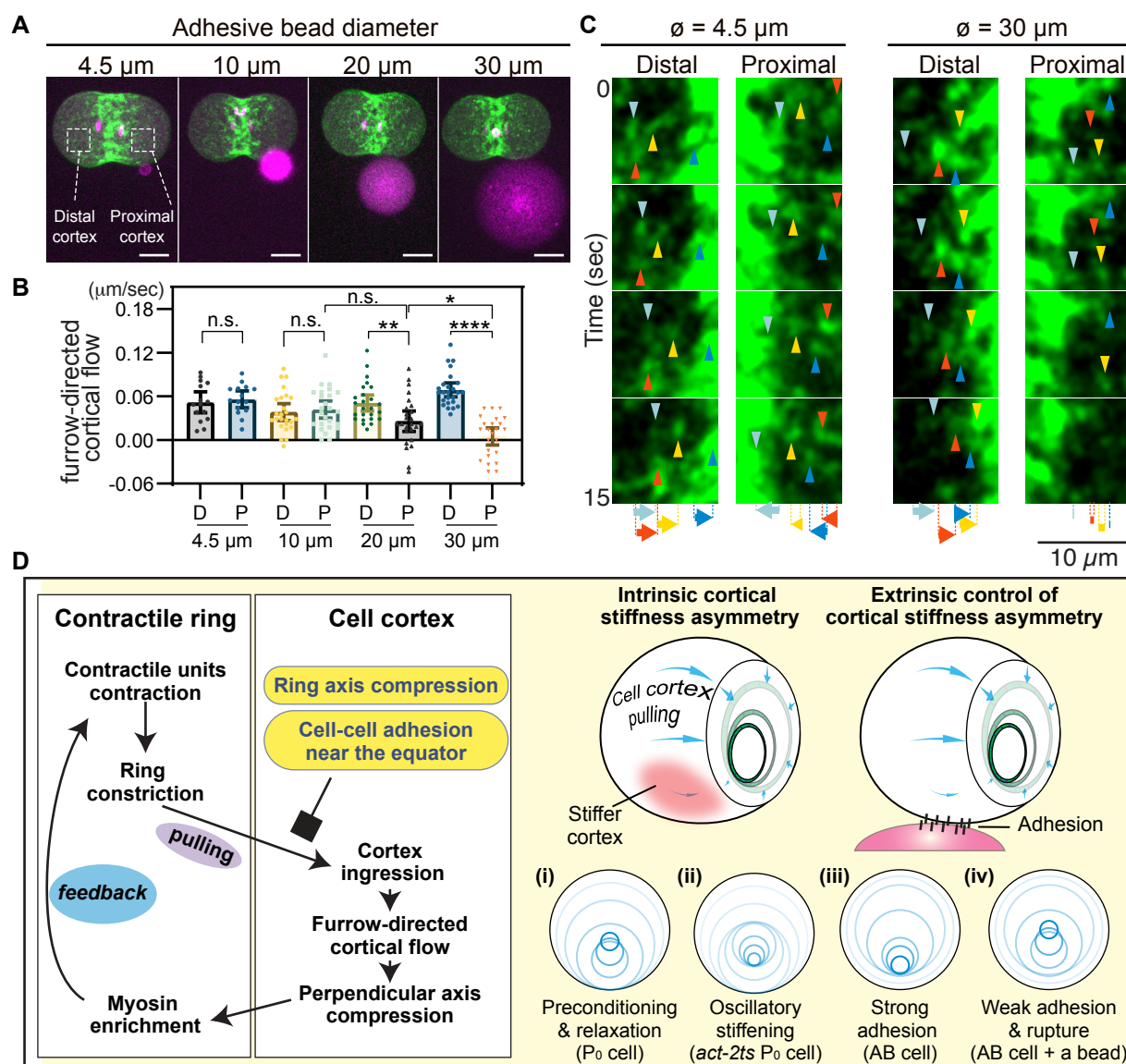


**Figure 7. Adhesion inhibits furrow-directed cortical flow.**

(A) Isolated AB cells attached to adhesive beads of different diameters. (B) Furrow-directed cortical flow proximal (P) and distal (D) to bead attachment sites. (C) Myosin movement with a bead attached. Arrowheads indicate myosin foci. Arrows below micrographs indicate total displacements over 15 sec. (D) Working hypothesis for symmetry-breaking in unilateral cytokinesis. Ring-axis compression and cell-cell adhesion inhibit cortical ingression and furrow-directed cortical flow by suppressing ring-dependent cortex pulling (left diagram). Perpendicular-axis compression in wild-type embryos is a result of furrow-directed cortical flow that induces myosin enrichment at the equatorial cortex through compression-dependent feedback. Suppression of cell cortex pulling induces unilateral cytokinesis with and without the compression-dependent feedback. Cortical stiffness asymmetry induced by intrinsic cortical dynamics and external adhesion is the symmetry-breaking cue (right diagram). Differences in ring trajectories can be explained by differences in the timing of stiffness change (diagrams i-iv, lower right panel). Error bars indicate 95% confidence intervals. Scale bars, 10  $\mu\text{m}$ . p-values were calculated by one-way ANOVA with Holm-Sidak's multiple comparison test.



# Figure S1 (Hsu, Sangha, Fan, et al.)

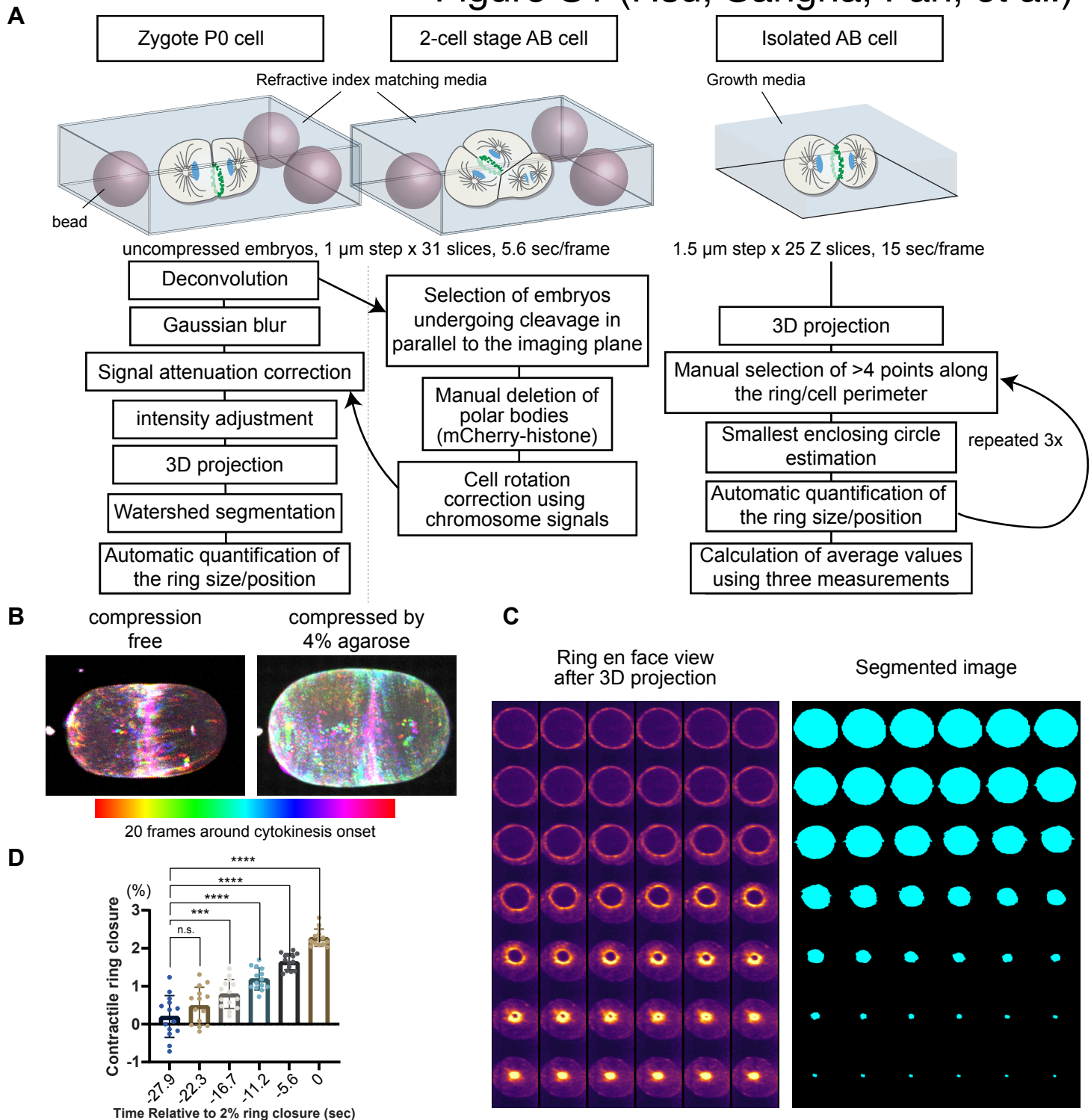
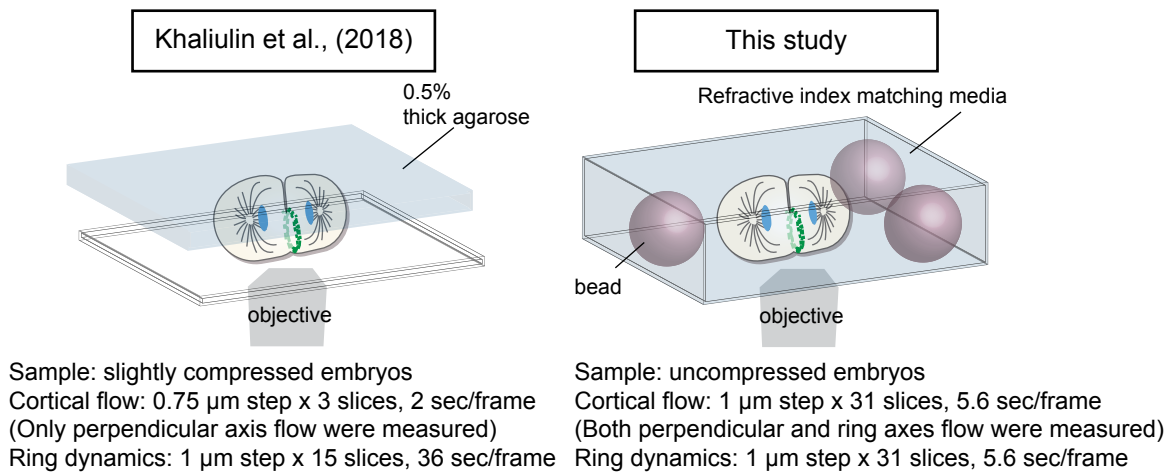


**Figure S1. Imaging and contractile ring analysis methods.**

(A) Imaging conditions and analytical flow charts. For intact embryos, we used refractive index matching medium and polystyrene beads as spacers. For isolated AB blastomeres, we used a normal growth medium and a different analytical pipeline to estimate ring size and position because of the cells' movement and rotation. Isolated AB cells were measured three times, and average values were analyzed. (B) Temporal color-coded image of 20 frames around cytokinesis onset showing that compression-free embryos do not exhibit global cortical rotation. (C) Ring en face view after the rotation of 3D projected data and ring segmentation. (D) Contractile ring closure data after alignment of time series data relative to 2 % ring closure. Error bars indicate 95% confidence intervals.

# Figure S2 (Hsu, Sangha, Fan, et al.)

**A**



**B**

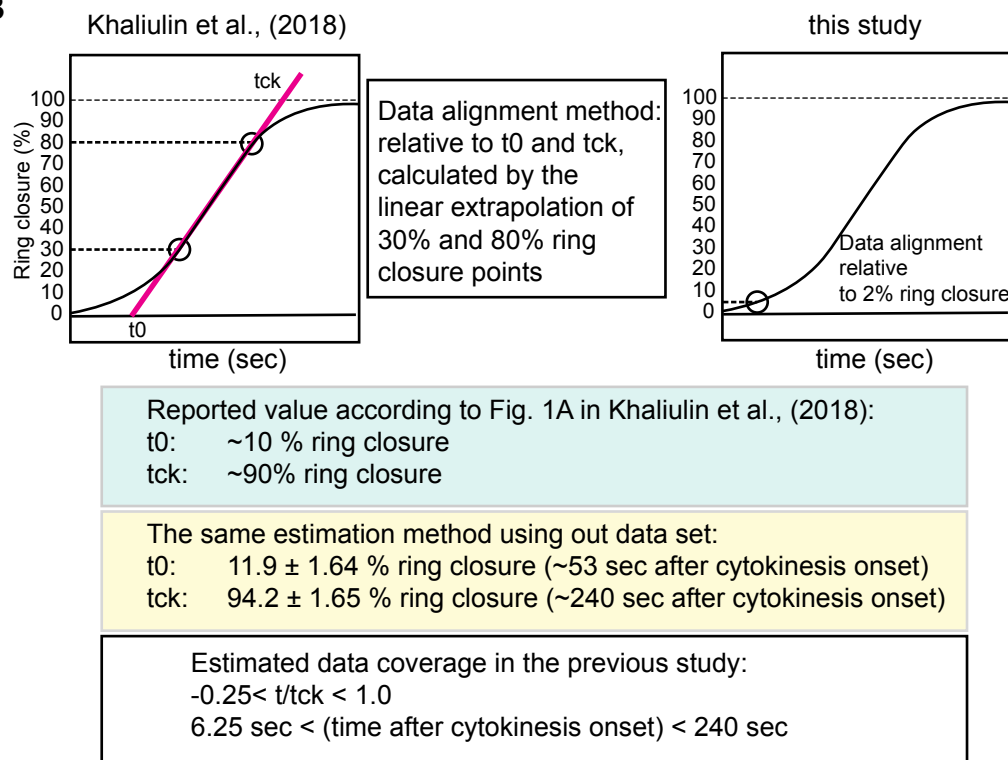
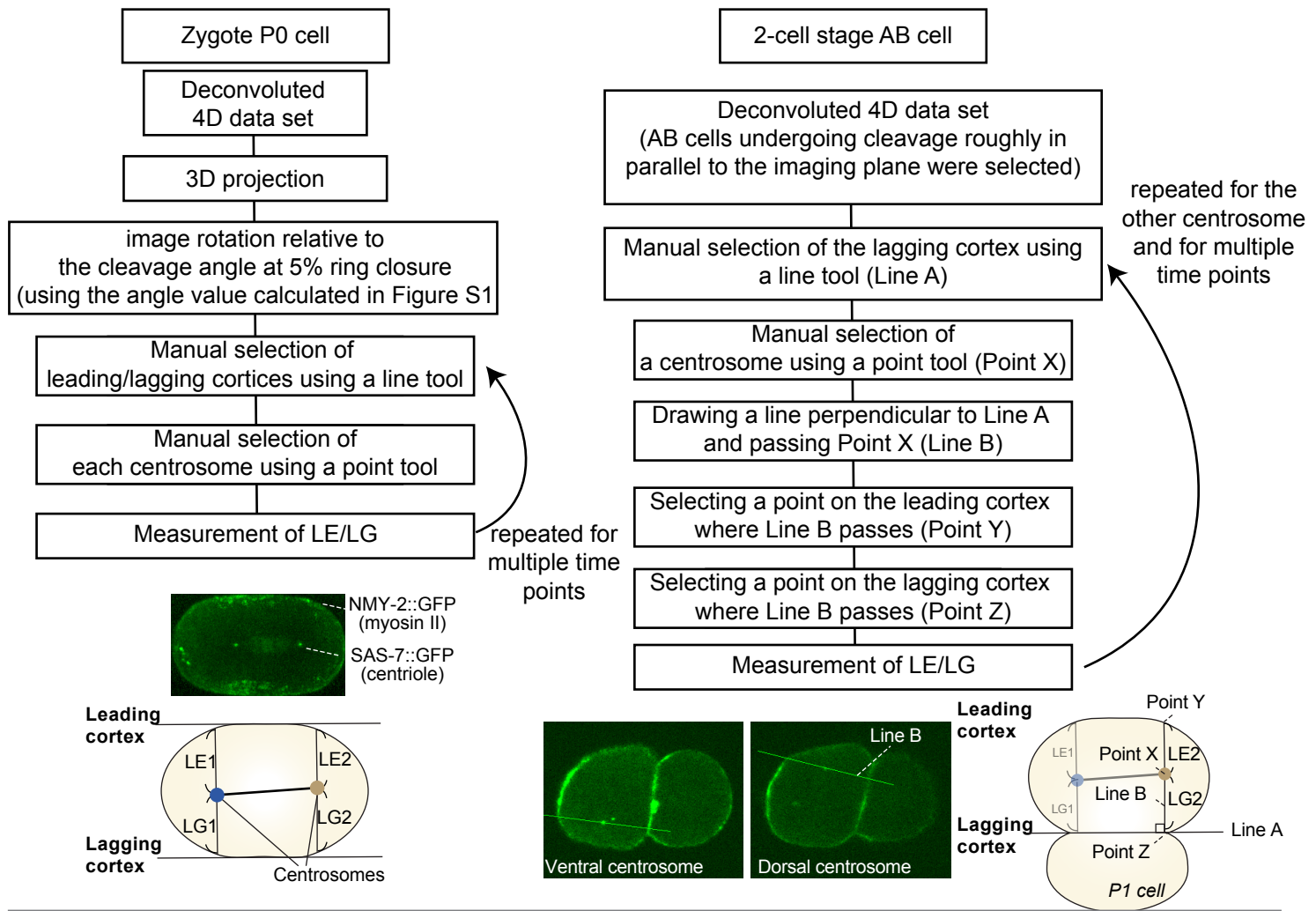


**Figure S2. Comparison between our methods and those of Khaliulin et al. (2018).**

(A) Left, a previous study by Khaliulin et al. used 0.5% thick agarose to mitigate compression, while our method does so using beads. Our data have increased spatial-temporal information regarding ring dynamics, while our axial and temporal resolution of cortical flow is lower. Nevertheless, the perpendicular-axis cortical flow data are highly reproducible and in good agreement with those of Khaliulin et al. (B) Left, Khaliulin et al. aligned data using a line passing through the 30% and 80% ring closure points. By linear extrapolation of the line to 100 and 0, tck and t0 were defined (red line). According to the paper, t0 and tck corresponded to 10% and 90% ring closure, respectively. Right, in our study, we aligned time-series data relative to 2% ring closure point to focus on earlier symmetry-breaking events. Using the method used by Khaliulin et al., t0 and tck in our data set are nearly identical at 11% and 94%, respectively. The time range of data reported by Khaliulin et al. was  $-0.25 t/tck$  to  $1.0 t/tck$  ( $= tck$ ), which is between 6.25 sec and 240 sec after cytokinesis onset based on our estimation. On the other hand, our data also includes 50–80 sec before cytokinesis onset.

# Figure S3 (Hsu, Sangha, Fan, et al.)

**A**



**B**

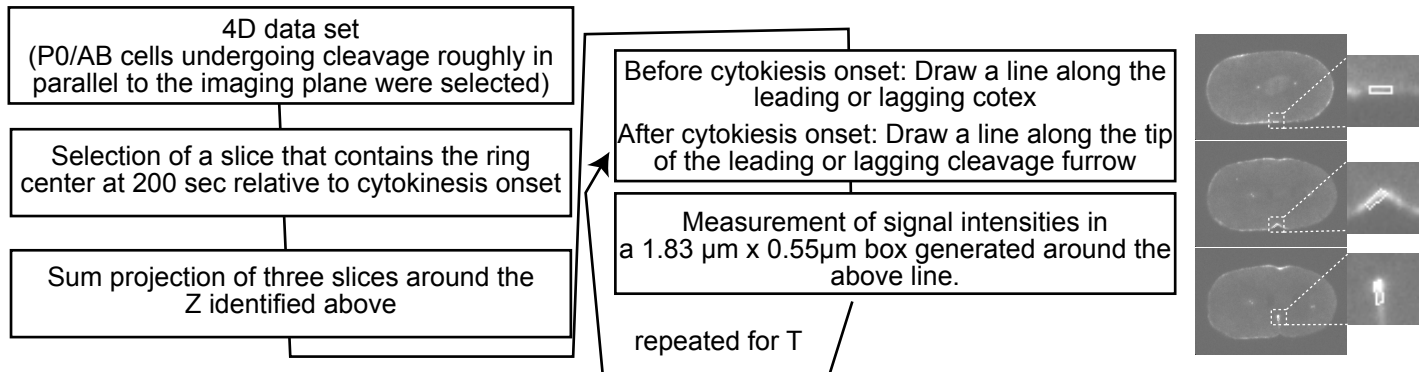


**Figure S3. Measurement of centrosome positioning and signal intensity.**

(A) Image analysis pipelines for P0 (left) and AB (right) spindle positioning. All processes were performed semi-automatically using in-house image J macros. (B) Image analysis pipeline for active RhoA and myosin signal intensities. White boxes in the insets of images on the right show the areas of measurement.